TU Delft

Delft University of Technology

Licence
CC BY

Citation (APA)
Maiti, S., Avis, G., Kar, S., & Wehner, S. (2026). Requirements for teleportation in an intercity quantum network. *New Journal of Physics*, *28*(10), Article 104515. https://doi.org/10.1088/1367-2630/aeb40a

Important note
To cite this publication, please use the final published version (if applicable).
Please check the document version above.

Copyright
In case the licence states “Dutch Copyright Act (Article 25fa)”, this publication was made available Green Open Access via the TU Delft Institutional Repository pursuant to Dutch Copyright Act (Article 25fa, the Taverne amendment). This provision does not affect copyright ownership.
Unless copyright is transferred by contract or statute, it remains with the copyright holder.

Sharing and reuse
Other than for strictly personal use, it is not permitted to download, forward or distribute the text or part of it, without the consent of the author(s) and/or copyright holder(s), unless the work is under an open content license such as Creative Commons.

Takedown policy
Please contact us and provide details if you believe this document breaches copyrights.
We will remove access to the work immediately and investigate your claim.

*This work is downloaded from Delft University of Technology.*

New Journal of Physics
The open access journal at the forefront of physics

Deutsche Physikalische Gesellschaft DPG IOP Institute of Physics

PAPER • OPEN ACCESS

# Requirements for teleportation in an intercity quantum network

To cite this article: Soubhadra Maiti *et al* 2026 *New J. Phys.* **28** 104515

View the article online for updates and enhancements.

You may also like

- Theory of relativistic surface plasmon excitation on smooth surfaces by high-intensity lasers
Bifeng Lei, Bin Qiao, Matt Zepf et al.
- Non-Hermitian Rayleigh–Schrödinger-like perturbation theory at exceptional point
Wei-Ming Chen and Chia-Yi Ju
- Model predictive quantum control: a modular approach for efficient and robust quantum optimal control
Eya Guizani and Julian Berberich

4-CHANNEL CONFIGURABLE OPEN RF ENGINE FOR QUANTUM EXPERIMENTS

LUGUS
Developed by Instrumentation Technologies

High bandwith arbitraty waveform generator (AWG)
Up to 1.25 GSPS

Open & programmable
Full access to FPGA implementation and firmware

Compatible with control frameworks
LabScript, ARTIQ, etc.

High power outputs
Up to 36 dBm

High-bandwidth feedback control
Open or closed-loop operation, Feedback bandwidth up to 125 MSPS

This content was downloaded from IP address 145.90.33.6 on 09/11/2026 at 11:53

New Journal of Physics
The open access journal at the forefront of physics

Deutsche Physikalische Gesellschaft DPG
IOP Institute of Physics

Published in partnership with: Deutsche Physikalische Gesellschaft and the Institute of Physics

Check for updates

PAPER

# Requirements for teleportation in an intercity quantum network

**Soubhadra Maiti**[1,2,3,*], **Guus Avis**[1,2,3,4], **Sounak Kar**[1,2,3] and **Stephanie Wehner**[1,2,3]

[1] QuTech, Delft University of Technology, Delft, Netherlands
[2] Kavli Institute of Nanoscience, Delft University of Technology, Delft, Netherlands
[3] Quantum Computer Science, Department of Electrical Engineering, Mathematics and Computer Science, Delft University of Technology, Delft, Netherlands
[4] Manning College of Information and Computer Sciences, University of Massachusetts Amherst, Amherst, MA, United States of America
[*] Author to whom any correspondence should be addressed.

**E-mail:** s.maiti-1@tudelft.nl

**OPEN ACCESS**

**RECEIVED**
17 June 2026

**REVISED**
7 September 2026

**ACCEPTED FOR PUBLICATION**
16 September 2026

**PUBLISHED**
27 October 2026

**Keywords:** quantum networks, quantum repeater, quantum teleportation

Supplementary material for this article is available online

Original content from this work may be used under the terms of the Creative Commons Attribution 4.0 licence.

Any further distribution of this work must maintain attribution to the author(s) and the title of the work, journal citation and DOI.

## Abstract

We investigate the hardware requirements for quantum teleportation in an intercity-scale network topology consisting of two metropolitan-scale networks connected via a long-distance backbone link. Specifically, we identify the minimal improvements required beyond the state-of-the-art to achieve an end-to-end expected teleportation fidelity of 2/3, which represents the classical limit. To this end, we formulate the hardware requirements computation as optimisation problems, where the hardware parameters representing the underlying device capabilities serve as decision variables. Assuming a simplified noise model, we derive closed-form analytical expressions for the teleportation fidelity and rate when the network is realised using heterogeneous quantum hardware, including a quantum repeater chain with a memory cut-off. Our derivations are based on events defined by the order statistics of link generation durations in both the metropolitan networks and the backbone, and the resulting expressions are verified against NetSquid simulations. The analytical expressions facilitate efficient exploration of the optimisation parameter space without resorting to computationally intensive simulations. We then apply this framework to a representative realisation in which the metropolitan nodes are based on trapped-ion processors and the backbone is composed of ensemble-based quantum memories. Our results suggest that teleportation across metropolitan distances already reaches the classical limit with state-of-the-art hardware when the data qubit is prepared after end-to-end entanglement has been established, whereas extending teleportation to intercity scales requires additional, though plausibly achievable, improvements in hardware performance.

## 1. Introduction

Quantum networks are anticipated to facilitate tasks beyond the reach of the classical internet [1]. In such networks, remote entanglement serves as the primary resource for a wide range of applications, including quantum key distribution (QKD) [2, 3], enhanced sensing [4], secure remote computation [5], clock synchronisation [6], and many other applications. Furthermore, entanglement shared across spatially separated locations enables foundational tests of quantum mechanics, most notably Bell inequality violation [7], as well as recent proposals for probing quantum gravity effects [8], among others. A remote entangled state consists of a pair of entangled qubits shared between end nodes, i.e. quantum devices directly accessible to users. The quality of service for any such application depends on the quality of these links, typically represented by the entanglement fidelity, and the rate at which they are generated. Furthermore, the required thresholds for these performance metrics vary with the underlying application, motivating a careful analysis of these metrics in realistic network architectures.

© 2026 The Author(s). Published by IOP Publishing Ltd on behalf of the Institute of Physics and Deutsche Physikalische Gesellschaft

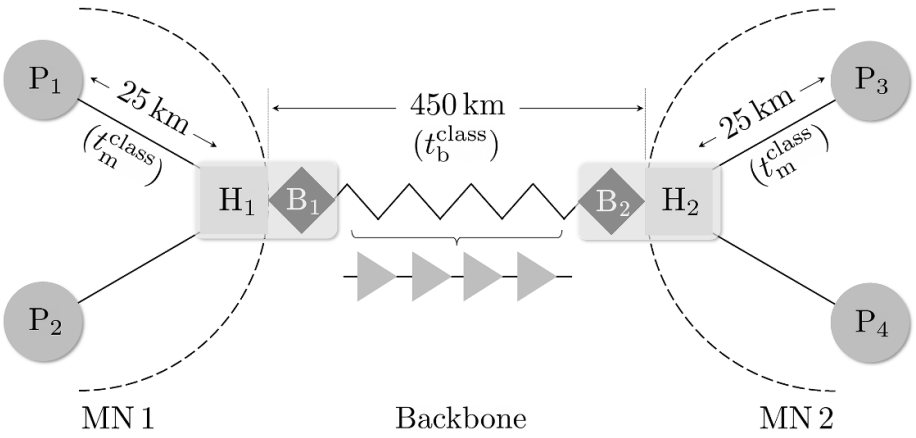



**Figure 1.** Schematic of an intercity quantum network architecture comprising four different components. User-controlled end nodes are denoted by circles $P_1$–$P_4$ and metropolitan hubs by squares $H_1$–$H_2$. The border nodes, shown as diamonds $B_1$–$B_2$, form the backbone together with the zig-zag line, which can be realised using either a space-based quantum channel or a terrestrial linear quantum repeater chain, with individual repeater nodes depicted as triangles. Each end node is connected to its nearest hub 25 km away and forms a metropolitan network (MN 1 or 2). The 450 km backbone connects the metropolitan regions via the border nodes at both ends. Together, the MNs and the backbone form the full intercity network, enabling long-distance quantum communication between multiple end nodes.

Photon transmission through optical fibre decays exponentially with propagation distance due to attenuation losses, which limits the feasibility of entanglement generation over long distances via direct photon transmission. Moreover, the no-cloning theorem [9] forbids the creation of identical copies of an unknown quantum state, making classical amplification techniques infeasible for quantum states. To overcome this, quantum repeaters [10] introduce intermediate nodes that enable entanglement distribution over extended distances. Entanglement generation has been experimentally demonstrated across various physical platforms, including trapped ions [11, 12], colour centres in solids [13], rare-earth ions [14], and atomic ensemble memories [15], where matter–photon entanglement is used to generate entanglement between distant matter qubits located at remote nodes. These platforms exhibit distinct advantages and limitations, and future large-scale quantum networks are therefore envisioned to adopt a heterogeneous architecture that integrates multiple hardware platforms [16–18].

One of the central challenges in realising a scalable quantum network lies in identifying the precise hardware requirements to support efficient quantum communication. Experimentally, Pompili *et al* [19] demonstrated a lab-scale three-node quantum network based on nitrogen-vacancy centres in diamond, while Krutyanskiy *et al* [12] proposed a quantum repeater node based on trapped ions capable of distributing entanglement over distances up to 50 km, marking significant experimental milestones. On the theoretical side, the performance of single-repeater setups and homogeneous repeater chains has been studied extensively, both analytically [20–22] and via simulation [23, 24]. However, to the best of our knowledge, performance analyses of heterogeneous repeater chains have so far relied predominantly on simulation-based approaches [24].

In the context of quantum networks, quantum teleportation serves both as a fundamental primitive and as a high-level performance benchmark. Applications such as blind quantum computing impose stringent requirements on teleportation fidelity and rate to ensure correctness and security [25]. Beyond its direct use for communication, teleportation constitutes a key resource for implementing non-local gates, thereby enabling the preparation of multipartite entangled states and distributed quantum information processing [26]. At the network level, the achievable end-to-end teleportation fidelity provides a quantitative measure of overall network performance [27]. Moreover, achieving a teleportation fidelity above the classical limit of $2/3$ demonstrates performance that no classical measure-and-prepare strategy can reproduce [28], analogous to Bell-inequality tests [29].

In this work, we investigate the requirements for quantum teleportation in an *intercity-scale network* (IN) shown in figure 1, consisting of two *metropolitan-scale networks* (MNs) and a long-distance *backbone* realised as a quantum repeater chain. A detailed description of the network model is provided in section 3. We adopt standard assumptions, including heralded entanglement generation (HEG), depolarising noise in memory, instantaneous local operations, swap-as-soon-as-possible (swap-ASAP) policy [30], and a cut-off strategy, together with the standard deterministic teleportation protocol, which succeeds with unit probability [31]; see **A1**–**A10** for details. Specifically, we study the requirements for attaining a teleportation fidelity of $2/3$ across metropolitan and intercity distances and carry out our

analysis in a hardware-agnostic manner, i.e. we characterise the network using a set of parameters capturing the essential hardware properties. The threshold 2/3 is the classical benchmark for qubit teleportation and is used here as a minimal criterion for demonstrating performance beyond any classical measure-and-prepare strategy. Exceeding this threshold does not, by itself, imply suitability for demanding applications that require substantially higher fidelities. Our results should therefore be interpreted as identifying the minimum hardware improvements required to achieve the classical limit. Higher targets can be incorporated in the same optimisation framework and would lead to more stringent requirements. To illustrate this, we additionally determine the requirements for a target fidelity of 0.77, chosen as the midpoint between the classical limit and 0.87, the highest expected teleportation fidelity attainable across the IN when every hardware parameter takes the best possible value we consider realistic in the near term.

To study the requirements, we focus on two teleportation scenarios that capture different operational regimes:

- **Entanglement-ready (ER)**: in ER teleportation, the data qubit (qubit to be teleported) is prepared only after end-to-end entanglement has been established. This approach allows the system to avoid the decoherence accumulated during the probabilistic entanglement generation process, thereby significantly improving teleportation fidelity [32].
- **Qubit-ready (QR)**: the data qubit is prepared in advance and stored in memory until end-to-end entanglement is established. Such situations can arise when the data qubit is produced by an external process, when the data qubit preparation rate is not synchronised with the entanglement generation rate [33], or when the network is used as a communication primitive for higher-level distributed protocols [1]. In such cases, the data qubit must remain in memory while the end-to-end entangled link is being generated, leading to additional decoherence. Thus, QR teleportation represents a more demanding operational regime than ER and provides a conservative yet useful test case for hardware requirements. Although we assume instantaneous local operations and qubit preparation (see **A10**), the QR scenario remains relevant.

In contrast to previous NetSquid-based studies on hardware requirements [23, 24, 34], we consider an IN employing heterogeneous hardware for the metropolitan and long-distance backbone segments and identify their independent hardware requirements. To the best of our knowledge, this is the first study for teleportation in such a setting. In order to determine these requirements, we formulate the task as an optimisation problem with the relevant cost function designed along the lines of [24]. To solve the resulting formulation, we first derive closed-form analytical expressions for the expected fidelities and generation rates of both the end-to-end link and teleported qubit and validate their accuracy against empirical estimates from NetSquid simulations [35]. These analytical expressions enable us to efficiently explore the parameter space and identify the requirements without resorting to computationally expensive simulations. Furthermore, to quantify the requirements, we introduce two reference values for each network parameter: the *baseline* value representing state-of-the-art hardware capabilities or estimates based on current experiments, and the *optimistic* value, representing near-term capabilities anticipated from ongoing experimental advances and theoretical predictions. We define the hardware requirements as the *minimal improvements* over the baseline needed to reach the target teleportation fidelity of 2/3. Since this criterion focuses only on fidelity, it is possible that the resulting ER and QR points correspond to substantially different rates. To ensure a *fair* comparison, we additionally impose a target rate and obtain parameter combinations that satisfy both the target fidelity and rate. In our analysis, we set the target rate to the rate achieved by the minimal-cost hardware configuration identified for the QR case. Although our framework itself is hardware-agnostic, we evaluate the requirements using a representative realisation of a network architecture comprising trapped-ion processors in the MN and a repeater chain based on ensemble-based memories in the backbone [17], along with corresponding baseline and optimistic parameter sets.

*Summary of results:* We specifically address the following questions with respect to hardware requirements:

**Q1** Do the baseline parameters reach the classical benchmark of 2/3 for teleportation fidelity in an MN? If not, what are the minimal improvements required?
- We find that current trapped-ion technology (baseline) already reaches the classical benchmark for ER teleportation at metropolitan scales, whereas QR teleportation requires improvement and reaches the benchmark with near-term experimental advances; see section 6.1 for details.

**Q2** Assuming that the backbone attains optimistic performance, what minimal improvements to the MN parameters are required to achieve an expected teleportation fidelity of $2/3$ across the IN? This analysis reveals the trade-offs among metropolitan parameters and provides a lower bound on their required improvements.
- We find that although ER teleportation reaches the target fidelity, QR teleportation requires significant improvement, which nonetheless remains within the reach of optimistic estimates. We also identify the feasible regions in parameter space and the optimal parameter configurations that minimise the hardware cost; see section 6.2 for details.

**Q3** Conversely, assuming optimistic MN performance, what are the corresponding backbone requirements for an expected teleportation fidelity of $2/3$ across the IN? This highlights the trade-offs among backbone parameters and establishes a lower bound on their required improvements.
- Similar to **Q2**, we find that ER teleportation reaches the target fidelity and QR teleportation requires significant improvements but is still within the reach of optimistic estimates; see section 6.2 for details.

**Q4** With baseline parameters for both the MN and backbone, what minimal joint improvements are needed to achieve an expected teleportation fidelity of $2/3$ in the IN?
- In this case, neither ER nor QR teleportation is possible at baseline, and we identify the minimal joint improvements; see section 6.2 for details.

Furthermore, in **Q1**–**Q4**, we observe that to achieve the same rate as the optimal configuration in QR teleportation, the ER case requires improvement over the baseline, though markedly less than in the QR scenario. Finally, we repeat the analysis corresponding to **Q1**–**Q4** for a higher target fidelity of 0.77. The required improvements become more demanding. While the elementary link generation probabilities are still driven to their optimistic values in all QR cases, the relative importance of the backbone parameters shifts from link generation probability to link fidelity; see section 6 for details.

Beyond their role in optimisation, the analytical expressions and the underlying methodology can also be used to evaluate performance metrics for heterogeneous networks and are therefore of independent interest.

The rest of this paper is organised as follows. First, we review relevant literature in section 2, followed by a description of the network setup and assumptions in section 3. Section 4 presents the objectives and methodology. In section 5, we derive analytical expressions for the teleportation rate and expected fidelity for the IN. Evaluations addressing **Q1**–**Q4** are presented in section 6 and the conclusions are drawn in section 7.

## 2. Related work

We begin by surveying prior work closely related to ours. This is not intended to be an extensive review of performance analyses of quantum repeater chains; instead, we focus on key contributions directly relevant to our setting. In this context, commonly considered performance metrics include the end-to-end entanglement generation time, fidelity, and secret key rate [36]. A substantial body of work derives closed-form or recursive expressions for entanglement generation in *homogeneous* chains under various swapping schedules and decoherence models [30, 37, 38], with Rozpedek *et al* [22] identifying the parameter regimes in which a single sequential repeater outperforms direct transmission. Another line of work addresses the rate-fidelity trade-off induced by memory cut-off policies, e.g. Li *et al* [39] optimise cut-off strategies for entanglement quality, Goodenough *et al* [20] obtain exact formulas and tight approximations for the expected fidelity under global cut-off and swap-ASAP policies, and Andrade *et al* [21] give closed-form end-to-end fidelities for sequential swapping. Multiplexed architectures [40] reduce the sensitivity of these figures of merit to memory coherence time. However, these frameworks do not extend directly to inhomogeneous repeater chains where the distances between nodes vary. In this work, we analyse a four-node chain in which the two outer links are identical while the central link differs, thereby enabling heterogeneous hardware, and derive exact expressions for the expected end-to-end fidelity and rate of both entanglement generation and teleportation under a cut-off policy, with classical communication delays fully accounted for.

Several proposals for quantum repeaters are based on atomic ensemble memories following the DLCZ protocol [41]. These schemes have been extended to incorporate multimode memories in rare-earth-doped solids and active purification to suppress multi-excitation noise [42, 43], systematically surveyed and benchmarked against direct transmission in [44], and further refined to account for time-dependent memory decay [45]. Matter-based alternatives include trapped ions [12, 46, 47], neutral atoms [48], rare-earth-doped crystals [49], and colour centres [50], while more recent work explores hybrid nodes combining ensemble-based repeaters with single-atom or ion-based processors [16–18], satellite-assisted links [51], and all-photonic repeaters [52]. Closest to our setting is the trapped-ion repeater node of Krutyanskiy *et al* [12], which swaps entanglement over two 25 km fibres and outlines a path to an 800 km chain. However, they assume that the memory coherence time significantly exceeds the elementary link generation time and therefore ignore memory decoherence, which is precisely the assumption we relax. Our analysis is platform-agnostic, and for numerical evaluation we adopt parameters from experimental implementations with trapped ions [12, 53–55] and predictions from [17]; see section 4.2 for details.

Finally, we review prior studies most relevant to our work that address the hardware specifications required for efficient quantum communication. A critical challenge in realising quantum repeaters is that their hardware requirements remain largely unknown. Silva *et al* [23] introduced a systematic approach using genetic algorithms and NetSquid simulations to identify minimal requirements for entanglement generation in repeater chains. As related works, Avis *et al* [24] and van Dam *et al* [56] determine the requirements for verifiable blind quantum computing (VBQC) over a single repeater and a 50 km direct link, respectively, using hardware-specific models of colour centres and trapped ions on real-world fibre grids. Subsequently, Silva *et al* [34] extended this to a 900 km homogeneous multi-repeater chain that enables VBQC and QKD. In contrast to these works, we consider an IN architecture in which MNs are connected by a backbone via border nodes, allowing us to separately quantify the requirements imposed on the two segments. While these works rely on simulations, we derive exact analytical expressions for teleportation rates and expected fidelities to carry out the analysis. Furthermore, instead of using theoretical limits as upper bounds, we impose optimistic near-term estimates based on ongoing experimental and theoretical advances for each hardware parameter. On this basis, we identify the minimal requirements in terms of coherence time, elementary link generation probability, and link fidelity needed to reach the classical fidelity threshold of $2/3$ for teleportation in an MN over 50 km and across an IN over 500 km; see figure 1.

## 3. Setup and assumptions

In this section, we briefly introduce the quantum network setup of [57], specify the hardware parameters that characterise it, and state the assumptions underlying our analysis, thereby enabling us to address **Q1**–**Q4**. Figure 1 shows a schematic of the network, comprising four fundamental components: end nodes, metropolitan hubs, a backbone, and border nodes, each serving distinct functions to enable scalable quantum communication. Since we analyse teleportation over metropolitan (up to 50 km) and intercity-scale (up to 500 km) distances, these components require capabilities beyond the minimal specifications for the devices provided in [57].

The *end nodes*, labelled $P_1$–$P_4$ in figure 1, serve as primary access points at which users run quantum applications under their own control. These devices generate matter–photon entanglement and support quantum processing capabilities, such as measurement and gate operations on matter qubits. For deterministic teleportation, we additionally require two quantum memories per end node and the ability to execute classical coordination and computing protocols. Recent experiments [19, 53, 58] have demonstrated promising platforms for such end nodes, achieving long coherence times and high quantum gate fidelities using colour centres, trapped ions, and neutral atoms.

Each end node is connected to a *metropolitan hub*, labelled $H_1$–$H_2$ in figure 1, which serves as a central point for facilitating HEG between node pairs within an MN over city-scale distances up to 50 km. End nodes $P_1$ and $P_2$ together with hub $H_1$ constitute MN 1, while end nodes $P_3$ and $P_4$ with hub $H_2$ constitute MN 2. To generate and route entanglement between different pairs of nodes, these hubs may comprise entanglement generation switches [59] or entanglement distribution switches [60]. For entanglement generation and teleportation, we only require that the hubs contain beam splitters and photon detectors for Bell state measurements (BSMs) on incoming photons. End nodes are connected to their hub via standard telecommunication fibres supporting photonic qubit transmission.

To overcome the distance limitations imposed by fibre loss, the architecture incorporates a long-range *backbone*, denoted by the zigzag line in figure 1, together with *border nodes* $B_1$ and $B_2$. These

**Table 1.** List of parameters.

| | |
|---|---|
| *Common parameters* | |
| $p_{\mathrm{m}}^{0}$ | base efficiency, i.e. the success probability of an entanglement generation attempt between two end nodes (or an end and border node) at zero separation |
| $d_{\mathrm{m}'}$ | distance between an end node and nearby metropolitan hub |
| $t_{\mathrm{prep}}$ | (constant) average duration of all local experimental overhead in a photon generation attempt from an end or border node |
| $t_{\mathrm{coh}}$ | memory coherence time of an end or border node |
| $t_{\mathrm{cut}}$ | cut-off time, i.e. the maximum allowable time between the earliest and latest generated links |
| $t_{\mathrm{msg}}$ | communication time between an end node and the farthest border node |
| *Metropolitan network parameters: end node to end node* | |
| $p_{\mathrm{m}'}$ | success probability of an entanglement generation attempt between two end nodes in an MN, i.e.$p_{\mathrm{m}'} = p_{\mathrm{m}}^{0} 10^{-2\alpha d_{\mathrm{m}'}/10}$; see (4) |
| $t_{\mathrm{m}'}$ | duration of an entanglement generation attempt between two end nodes in an MN |
| $f_{\mathrm{m}'}$ | fidelity of a freshly generated link between two end nodes in an MN,$f_{\mathrm{m}'} = (1+3w_{\mathrm{m}'})/4$, where $w_{\mathrm{m}'}$ is the corresponding Werner parameter |
| *Metropolitan network parameters: end node to border node* | |
| $p_{\mathrm{m}}$ | success probability of an entanglement generation attempt between an end and a neighbouring border node, i.e.$p_{\mathrm{m}} = p_{\mathrm{m}}^{0} 10^{-\alpha d_{\mathrm{m}'}/10}$; see (7) |
| $t_{\mathrm{m}}$ | duration of an entanglement generation attempt between an end and a neighbouring border node |
| $f_{\mathrm{m}}$ | fidelity of a freshly generated link between an end and a neighbouring border node,$f_{\mathrm{m}} = (1+3w_{\mathrm{m}})/4$, where $w_{\mathrm{m}}$ is the corresponding Werner parameter |
| *Backbone parameters* | |
| $p_{\mathrm{b}}$ | success probability of an entanglement generation attempt in the backbone |
| $t_{\mathrm{b}}$ | (constant) duration of an entanglement generation attempt in the backbone |
| $f_{\mathrm{b}}$ | fidelity of a freshly generated link in the backbone,$f_{\mathrm{b}} = (1+3w_{\mathrm{b}})/4$, where $w_{\mathrm{b}}$ is the corresponding Werner parameter |

nodes (referred to as junction nodes in [57]) are placed adjacent to the hubs and serve as interfaces between the backbone and MNs. Each border node contains at least two memories and has the same processing and storage capabilities as the end nodes, allowing it to store entanglement both with neighbouring end nodes and across the backbone. A key feature of this architecture is its ability to integrate heterogeneous quantum hardware platforms, thereby leveraging their distinct advantages, such as high-fidelity quantum gates, long memory coherence time, and multiplexing. The backbone itself may be realised by space-based links [61, 62] which offer low-loss photon transmission over long distances, or by a fibre-based multiplexed quantum repeater chain [16, 42, 44]. We define the IN as the composite architecture in which two distant MNs are connected via a backbone.

Throughout this paper, we use the terms *entanglement* and *link* interchangeably to denote an entangled state shared by two nodes. Furthermore, we model entanglement generation in the IN as a single-shot process: once a border node performs an entanglement swap, it remains idle until the ongoing end-to-end entanglement generation process completes. We refer to a complete trial to establish an end-to-end link as a *round*, while individual trials for elementary link generation are termed *attempts*. We assume time is slotted and derive all performance metrics accordingly. Under this framework, we analyse the performance of this architecture in a platform-agnostic manner, using a small set of parameters that describe the elementary links and node memories. We introduce these parameters following the physical structure of the network. For teleportation within an MN, the relevant elementary link is shared between two end nodes through a metropolitan hub and is characterised by the entanglement generation probability $p_{\mathrm{m}'}$, the fidelity $f_{\mathrm{m}'}$ of a freshly generated link, and the memory coherence time $t_{\mathrm{coh}}$ of the end nodes.

For intercity teleportation, we also refer to the link connecting an end node to its neighbouring border node as a metropolitan link. Hence, the end-to-end link comprises three links, namely, two metropolitan links and one backbone link. We assume a symmetric architecture in which the two MNs are identical (see A3), the end nodes are equidistant from their hubs, and border nodes have the same memory properties as end nodes. This assumption is not central to the methodology, which can be extended to asymmetric networks with heterogeneous nodes and unequal link distances, at the cost of introducing additional parameters. The metropolitan links are therefore characterised by the entanglement generation probability $p_{\mathrm{m}}$, the freshly generated link fidelity $f_{\mathrm{m}}$, and memory coherence time $t_{\mathrm{coh}}$, while the backbone link is characterised by its entanglement generation probability $p_{\mathrm{b}}$ and freshly generated link fidelity $f_{\mathrm{b}}$. Hence, the performance of the IN is governed by the five hardware parameters $p_{\mathrm{m}}$, $t_{\mathrm{coh}}$, $f_{\mathrm{m}}$, $p_{\mathrm{b}}$, and $f_{\mathrm{b}}$. The definitions of these parameters are summarised in table 1.

We now state the assumptions necessary to model the processes governing teleportation in the IN, from which we derive the expected teleportation fidelity and corresponding rate.

**A1** **Entangled state description**: We model all entangled states in the MN and backbone as Werner states [63]

$$\rho = w\left|\Phi^+\right\rangle\left\langle\Phi^+\right| + (1-w)\,\frac{\mathbb{I}_4}{4}\,, \tag{1}$$

where $|\Phi^+\rangle = (|00\rangle + |11\rangle)/\sqrt{2}$ is a maximally entangled Bell state, $w \in [0,1]$ is the Werner parameter, and $\mathbb{I}_4$ is the $4\times 4$ identity matrix. The fidelity of $\rho$ with respect to $|\Phi^+\rangle$ is $(1+3w)/4$. The choice of $|\Phi^+\rangle$ as the target Bell state is made without loss of generality since any Bell state can be transformed into another via local gate operations. In the double-click HEG protocol, different successful heralding patterns can correspond to different Bell states, or to states that are locally equivalent to a fixed Bell state. Since the heralding pattern is known, the corresponding local Pauli correction can be applied, so that the generated state can be represented as $|\Phi^+\rangle$.

While physically realised remote entangled states are generally not of Werner form [42, 47], the model is justified for the following reasons. First, swapping two Werner states yields a Werner state whose parameter is the product of the two input parameters [64], which simplifies the analysis. Second, any bipartite state can be transformed into a Werner state by twirling, i.e. by applying identical rotations on each qubit drawn uniformly at random from a set of operations [65].

**A2** **Noise in memory**: During entanglement generation across multiple links or in the presence of classical communication delays, the qubits stored in memory undergo decoherence. We model this noise as a depolarising channel. A state $\rho_A$ undergoing a depolarising channel $\mathcal{E}_t$ over a storage time $t$ in memory $A$ evolves as

$$\mathcal{E}_t(\rho_A) = \mathrm{e}^{-t/t_{\mathrm{coh}}}\rho_A + \left(1-\mathrm{e}^{-t/t_{\mathrm{coh}}}\right)\frac{\mathbb{I}_2}{2}\,, \tag{2}$$

where $t_{\mathrm{coh}}$ is the memory coherence time. Since a Werner state $\rho_{AB}$ has maximally mixed marginals, storing both qubits for duration $t$ gives

$$\mathcal{E}_t \otimes \mathcal{E}_t(\rho_{AB}) = \mathrm{e}^{-2t/t_{\mathrm{coh}}}\rho_{AB} + \left(1-\mathrm{e}^{-2t/t_{\mathrm{coh}}}\right)\frac{\mathbb{I}_4}{4}\,. \tag{3}$$

It is worth noting that on certain platforms, such as trapped-ion systems, memory noise can be more accurately described by correlated dephasing with a Gaussian temporal profile [12]. We nevertheless adopt the exponential depolarising channel (2) for analytical tractability and platform independence. Specifically, depolarising noise preserves the Werner form (1), thereby simplifying the analysis [20]. Moreover, while the depolarising channel does not accurately capture the correlated and non-Markovian nature of Gaussian dephasing, it captures the feature common to all these mechanisms, namely the monotonic degradation of the stored state with time [66]. It is thus a comparable benchmark across architectures rather than a hardware-exact model. A detailed analysis of such platform-specific noise models is left for future work.

**A3** **Symmetric metropolitan networks**: We assume that the two MNs are symmetric, such that the end nodes are equidistant from their hubs and border nodes have the same memory properties as end nodes. This keeps the analytics tractable and allows us to focus on the key trade-offs between the MN and backbone parameters. This assumption is not central to the methodology, as the same framework can be extended to asymmetric networks with asymmetric link properties and node properties at the cost of introducing additional parameters.

A4 **Entanglement generation between end nodes in a metropolitan network**: We adopt the double-click HEG protocol [67]. Specifically, to entangle two end nodes in an MN, e.g. $\mathrm{P}_1$ and $\mathrm{P}_2$ in MN 1 (figure 1), both nodes first generate matter–photon entanglement and send the photons to the midpoint hub, where a photonic BSM is performed. The outcome is communicated to both end nodes, heralding whether entanglement generation was successful. We further assume that attempts are made at fixed intervals, defined as the *cycle time*. Both the cycle time and success probability depend on the fibre length between the nodes.

Denoting the end node-to-hub distance by $d_{\mathrm{m}'}$, the fibre length between end nodes is $2d_{\mathrm{m}'}$. With fibre loss modelled by the exponential attenuation factor $\eta(\cdot)$ [34], the generation probability is

$$p_{\mathrm{m}'} = p_{\mathrm{m}}^0\ \eta\left(2d_{\mathrm{m}'}\right) = p_{\mathrm{m}}^0 10^{-2\alpha d_{\mathrm{m}'}/10}\,, \tag{4}$$

where $\alpha = 0.2\,\mathrm{dB\,km^{-1}}$ is the attenuation coefficient [46] of standard telecommunication fibre near 1550 nm, and $p_{\mathrm{m}}^0$, named base efficiency, captures all distance-independent factors, including source brightness, coupling loss, and visibility.

To derive the cycle time, i.e. the duration of each entanglement generation attempt, we observe that the propagation time for a photon from an end node to hub and the heralding signal back are each given by $t_{\mathrm{m}}^{\mathrm{class}} = d_{\mathrm{m}'}/v$, where $v$ is the speed of light in fibre. We take $v = c_0/n$, where $c_0 = 3 \times 10^5\,\mathrm{kms^{-1}}$ is the speed of light in vacuum and $n = 1.5$ is the refractive index of fibre. To account for other delays, we introduce $t_{\mathrm{prep}}$ as the average duration of all local (i.e. node-level) experimental overheads. This may, for example, represent intrinsic delays in trapped-ion systems, which arise from procedures such as laser excitation, qubit initialisation, cooling, optical pumping, and control latencies [12]. Thus, synchronised attempts give the cycle time

$$t_{\mathrm{m}'} = t_{\mathrm{prep}} + 2t_{\mathrm{m}}^{\mathrm{class}} \ . \tag{5}$$

Throughout, we express $t_{\mathrm{m}'}$, $t_{\mathrm{prep}}$, and $t_{\mathrm{m}}^{\mathrm{class}}$ in units chosen such that their numerical values are integers. In the resulting discrete-time analysis, the number of cycles $M'$ to establish a link is geometrically distributed,

$$M' \sim \mathrm{Geo}\,(p_{\mathrm{m}'}) \ , \tag{6}$$

and a freshly generated link is assumed to be of the Werner form (1) with fidelity $f_{\mathrm{m}'}$ and corresponding parameter $w_{\mathrm{m}'}$ such that $f_{\mathrm{m}'} = (1 + 3w_{\mathrm{m}'})/4$. Note that imperfections such as two-photon interference visibility, detector inefficiencies, or dark counts contribute to noise and consequently lower the fidelity. We do not model these effects explicitly and instead incorporate them into the effective fidelity $f_{\mathrm{m}'}$. This approach similarly applies to the assumptions outlined in A5–A6.

**A5** **Entanglement generation between an end node and a neighbouring border node**: Similar to A4, we adopt a discrete-time model for entanglement generation, now between an end node and a neighbouring border node, e.g. between $\mathrm{P}_1$ and $\mathrm{B}_1$. We also refer to such links as metropolitan links. Since $\mathrm{B}_1$ is located right next to the hub $\mathrm{H}_1$, only the photon from $\mathrm{P}_1$ traverses the distance $d_{\mathrm{m}'}$ to $\mathrm{H}_1$, while the propagation and heralding time from $\mathrm{B}_1$ is negligible. Furthermore, the border nodes are assumed to have the same properties as the end nodes such that the generation probability is

$$p_{\mathrm{m}} = p_{\mathrm{m}}^0 \eta\,(d_{\mathrm{m}'}) = p_{\mathrm{m}}^0 10^{-\alpha d_{\mathrm{m}'}/10} \ , \tag{7}$$

and with the same local overhead $t_{\mathrm{prep}}$ and synchronised attempts, the cycle time is

$$t_{\mathrm{m}} = t_{\mathrm{prep}} + 2t_{\mathrm{m}}^{\mathrm{class}} \ . \tag{8}$$

Finally, the number of attempts $M_i$ to generate link $i$ follows a geometric distribution,

$$M_i \sim \mathrm{Geo}\,(p_{\mathrm{m}}) \ , \quad i \in \{1,2\} \ . \tag{9}$$

Once an attempt succeeds, we assume that the generated link is of the Werner form (1) with fidelity $f_{\mathrm{m}}$ and corresponding parameter $w_{\mathrm{m}}$ such that $f_{\mathrm{m}} = (1 + 3w_{\mathrm{m}})/4$.

**A6** **Entanglement generation in the backbone**: We model entanglement generation in the backbone as a monolithic process, where each attempt takes a fixed duration $t_{\mathrm{b}}$ and succeeds with probability $p_{\mathrm{b}}$. This abstraction captures the behaviour of systems that can store spin qubits in memory, such as trapped ions and colour centres, as well as systems capable of storing photonic qubits for a finite time window, such as atomic ensemble-based memories. Thus, the number of attempts $M_{\mathrm{b}}$ required for link generation and the generation time $X_{\mathrm{b}}$ are

$$M_{\mathrm{b}} \sim \mathrm{Geo}\,(p_{\mathrm{b}}) \ , \quad X_{\mathrm{b}} := t_{\mathrm{b}} M_{\mathrm{b}} \ , \tag{10}$$

and the resulting entanglement generation rate is

$$R_{\mathrm{b}} = 1/\mathbb{E}\,(X_{\mathrm{b}}) = p_{\mathrm{b}}/t_{\mathrm{b}} \ . \tag{11}$$

Since we consider that the border nodes share the same properties as the end nodes, we again assign $t_{\mathrm{prep}}$ as the local overhead at a border node (see A4). Thus, we define the cycle time $t_{\mathrm{b}}$ as the sum

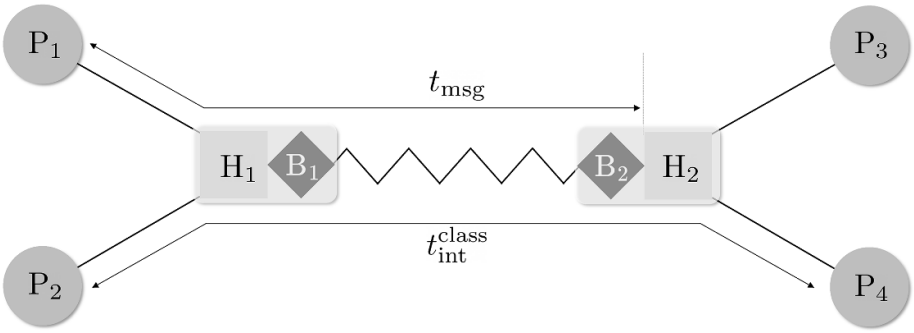



**Figure 2.** Classical communication time between nodes in an intercity quantum network (see A8).

of the local overhead $t_{\mathrm{prep}}$ and the one-way communication time between the two border nodes across the backbone $t_{\mathrm{b}}^{\mathrm{class}}$, i.e.

$$t_{\mathrm{b}} = t_{\mathrm{prep}} + t_{\mathrm{b}}^{\mathrm{class}} \ . \tag{12}$$

For evaluation, we use an estimate of the backbone link generation rate from a model of trapped-ion nodes connected via repeaters composed of ensemble-based memory [16]. Thus, we obtain $p_{\mathrm{b}}$ by using (11) and (12). Note that $t_{\mathrm{b}}$, $t_{\mathrm{prep}}$, and $t_{\mathrm{b}}^{\mathrm{class}}$ are expressed in units chosen such that their numerical values are integers. We also assume that the link in the repeater chain can be transferred to the border node memories without loss such that the resulting link can be described by a Werner state (1) with a parameter $w_{\mathrm{b}}$ and corresponding fidelity $f_{\mathrm{b}}$ such that $f_{\mathrm{b}} = (1+3w_{\mathrm{b}})/4$.

**A7** **Entanglement swapping**: End-to-end entanglement across the IN is created in two steps: first, links between end and border nodes and in the backbone are created in parallel, which we refer to as elementary links. We adopt the swap-ASAP policy [30], i.e. as soon as a border node holds entangled links on both sides, it performs an entanglement swap [31]. Two such swaps on two border nodes create an end-to-end link. We assume this swap is realised deterministically, since the border nodes can implement the swap using quantum gates and measurements on the memory qubits. Furthermore, we assume that the swap process is noiseless. This is justified in the context of long-range quantum teleportation, where qubit decoherence due to waiting times is the dominant source of noise.

**A8** **Classical communication time between nodes**: At the beginning of each round, all elementary links are attempted in a synchronised manner. After each swap, a classical message is sent to the end nodes to herald a successful swap. For the final swap, the message heralds the successful end-to-end entanglement generation. Since the border node is located adjacent to its hub, the communication delay from a border node to a neighbouring end node is $t_{\mathrm{m}}^{\mathrm{class}}$. Using $t_{\mathrm{b}}^{\mathrm{class}}$ as the propagation time across backbone (see A6), the final notification time is

$$t_{\mathrm{msg}} = t_{\mathrm{m}}^{\mathrm{class}} + t_{\mathrm{b}}^{\mathrm{class}} \ . \tag{13}$$

The total classical communication time between end nodes in different MNs is therefore

$$t_{\mathrm{int}}^{\mathrm{class}} = 2t_{\mathrm{m}}^{\mathrm{class}} + t_{\mathrm{b}}^{\mathrm{class}} \ . \tag{14}$$

See figure 2 for an illustration.

**A9** **Cut-off time**: Since elementary links are generated probabilistically, links generated early decohere while waiting for their neighbours. To mitigate this effect, a common strategy is to employ a cut-off mechanism [39], where old degraded links are discarded and replaced with freshly prepared links. In our single-shot model, we implement this strategy as follows: initiate all elementary link generation attempts simultaneously, a timer activates when the first link succeeds, and swaps are performed as adjacent links become available, provided the remaining links are established within the cut-off time $t_{\mathrm{cut}}$. Conversely, if all required links are not created within $t_{\mathrm{cut}}$, all active links are discarded, and the round restarts. This approach is commonly referred to as a *global cut-off* strategy in literature [20]. As mentioned earlier, we define a *round* as a whole trial to establish an end-to-end link,

**Table 2.** Description of quantities of interest and the influencing parameters.

| Quantities of interest | Influencing parameters |
|---|---|
| *Metropolitan network (MN)*: | |
| Teleportation rate $R_{\mathrm{m}}$ | $p_{\mathrm{m}}^{0}$ |
| Expected ER teleportation fidelity $F_{\mathrm{m}}^{\mathrm{ER}}$ | $t_{\mathrm{coh}}, f_{\mathrm{m}}{}'$ |
| Expected QR teleportation fidelity $F_{\mathrm{m}}^{\mathrm{QR}}$ | $p_{\mathrm{m}}^{0}, t_{\mathrm{coh}}, f_{\mathrm{m}}{}'$ |
| *Intercity network (IN)*: | |
| Teleportation rate $R_{\mathrm{int}}$ | $p_{\mathrm{m}}^{0}, p_{\mathrm{b}}, (t_{\mathrm{cut}})$ |
| Expected ER teleportation fidelity $F_{\mathrm{int}}^{\mathrm{ER}}$ | $p_{\mathrm{m}}^{0}, t_{\mathrm{coh}}, f_{\mathrm{m}}, p_{\mathrm{b}}, f_{\mathrm{b}}, (t_{\mathrm{cut}})$ |
| Expected QR teleportation fidelity $F_{\mathrm{int}}^{\mathrm{QR}}$ | $p_{\mathrm{m}}^{0}, t_{\mathrm{coh}}, f_{\mathrm{m}}, p_{\mathrm{b}}, f_{\mathrm{b}}, (t_{\mathrm{cut}})$ |

composed of multiple elementary link generation attempts. A round is considered successful if the interval between the earliest and latest elementary links remains below $t_{\mathrm{cut}}$.
While a lower cut-off time $t_{\mathrm{cut}}$ improves the end-to-end link fidelity by reducing storage times, it lowers the link generation rate, since more links are discarded. Following [24], we vary $t_{\mathrm{cut}}$ within the range

$$t_{\mathrm{cut}}/t_{\mathrm{coh}} \in [0.01, 1] \ , \tag{15}$$

where $t_{\mathrm{coh}}$ denotes the memory coherence time. Moreover, the cut-off time must be sufficiently large to accommodate the elementary cycle times $(t_{\mathrm{m}}, t_{\mathrm{b}})$ and the communication delay $(t_{\mathrm{msg}})$. Since we treat time as a discrete variable, taking values in the set of natural numbers, we have

$$t_{\mathrm{cut}} \in \left(\max\left\{t_{\mathrm{m}}, t_{\mathrm{b}}, t_{\mathrm{msg}}, 0.01\, t_{\mathrm{coh}}\right\},\ t_{\mathrm{coh}}\right] \cap \mathbb{N} =: T_{\mathrm{cut}} \ . \tag{16}$$

Note that our analysis in sections 5.1 and 5.2 only requires the lower bound of $t_{\mathrm{cut}}$, but not the upper bound. Also, cut-off times apply exclusively to HEG between end nodes involving multiple links, and the data qubits are never discarded.
Note that, as per our cut-off strategy, the decision to restart applies to all elementary links. However, it is possible to enhance the end-to-end rate by adopting more flexible cut-off strategies; for instance, one may discard and restart only those links whose generation time exceeds $t_{\mathrm{cut}}$, while retaining other successfully generated links. This process continues until all three links are generated within a $t_{\mathrm{cut}}$ time window. Analysing this cut-off policy is more involved and is left as future work.

**A10 Data qubit preparation, local gate operation, and qubit measurement**: Although the time scales of qubit initialisation, gate operations, and measurements vary across physical platforms, they are orders of magnitude shorter than the entanglement generation and classical communication times in networks spanning hundreds of kilometres. For example, qubit preparation, gates, and measurements typically range from hundreds of nanoseconds to a few microseconds in trapped-ion systems [24, 68], and in colour centres [32, 69, 70]. In contrast, classical communication across hundreds of kilometres incurs millisecond-scale delays, constrained by the speed of light in fibre (approx. $5\,\mu$s/km). Furthermore, remote entanglement generation typically requires multiple attempts due to probabilistic photon generation, fibre loss, detector inefficiencies, and probabilistic heralding, further increasing the overall generation time. Due to this pronounced separation of time scales, we treat the local operations as instantaneous. For the HEG process, we account for the local experimental overheads separately in A4, A5, and A6 via (5), (8), and (12), which can range from several hundred microseconds to milliseconds per attempt [12].

Equipped with these assumptions, we now describe the optimisation framework and methods.

## 4. Objectives and methods

We now present the methodology for determining the necessary requirements to achieve teleportation with a desired quality in the network shown in figure 1, addressing **Q1**–**Q4**. We observe that the rate and expected fidelities of ER and QR teleportation in the MNs and IN depend on the parameters as shown in table 2. In addition, we include the *non-hardware* parameter, cut-off time $t_{\mathrm{cut}}$ (in parentheses), to show its influence on the relevant performance metrics. Under our assumption of instantaneous local operations, the rates are identical for both teleportation types in the MN and IN. Our objective is

to identify the parameter combinations required to achieve the target teleportation fidelity $2/3$ in the MN and IN. Within the feasible parameter space, we seek to determine the minimal improvement over the baseline parameters with respect to the cost function defined below.

### 4.1. Optimisation framework and hardware cost

We recall from **Q1**–**Q4** that our first objective is to investigate whether the state-of-the-art hardware already achieves the target teleportation fidelity $f_{\text{target}}$; in the analysis, we consider two targets, $f_{\text{target}} = 2/3$ and $f_{\text{target}} = 0.77$. To that end, we characterise the feasible parameter range over which this threshold is attained. Let $\vec{\lambda}$ denote the generic hardware parameter vector determining the expected teleportation fidelity $F$ and rate $R$, where $F \in \{F_{\text{m}}^{\text{ER}}, F_{\text{m}}^{\text{QR}}, F_{\text{int}}^{\text{ER}}, F_{\text{int}}^{\text{QR}}\}$ and $R \in \{R_{\text{m}}, R_{\text{int}}\}$, respectively; see table 2 for the explicit forms. In addition, table 2 shows the dependence of $F$ on the *optional* non-hardware parameter $t_{\text{cut}}$. Denoting the feasible hardware parameter space as $\Lambda$ and the range of $t_{\text{cut}}$ as $T_{\text{cut}}$, the desired range is

$$\Lambda_{+} := \left\{ \vec{\lambda} \in \Lambda : \max_{t_{\text{cut}} \in T_{\text{cut}}} F\left(\vec{\lambda} \mid t_{\text{cut}}\right) \geqslant f_{\text{target}} \right\}, \text{ where } \Lambda := \times_{i=1}^{m} \left[ \underline{\lambda}^{(i)}, \overline{\lambda}^{(i)} \right] , \tag{17}$$

with $\underline{\lambda}^{(i)}$, $\overline{\lambda}^{(i)}$, and $m$ respectively denoting the lowest possible value of the $i$th hardware parameter, its optimistic value, and the number of parameters influencing $F$. The optimistic values represent projections by experimental groups for achievable performance in the near future; see section 4.2. Since these projections are based on current experimental status and anticipated room for improvement, it remains unclear *a priori* whether these values are sufficient to reach the target. Therefore, we impose $\overline{\lambda}^{(i)}$ as an upper bound in (17) to identify, if it exists, the most accessible point in the parameter space meeting the criterion. Note that the vertical bar preceding $t_{\text{cut}}$ in the expression for $F$ in (17) highlights it as a non-hardware parameter, relevant only to teleportation in the IN. The specific form of $T_{\text{cut}}$ is provided in (16). Furthermore, we define the baseline parameters $\underline{\lambda}^{(i)}$ as the current state-of-the-art values or corresponding estimates such that $\underline{\lambda}^{(i)} \in [\underline{\lambda}^{(i)}, \overline{\lambda}^{(i)}]$, for all $i$. In our evaluation, we specifically adopt the baseline and optimistic parameter sets corresponding to experiments with trapped-ion and ensemble-based memories; see section 4.2 for details.

It is evident that if the baseline parameters already lie in the desired range $\Lambda_{+}$, no further improvement is required. Otherwise, we aim to find the *minimal* improvements by restricting our search to

$$\Lambda_{++} := \left\{ \vec{\lambda} \in \Lambda_{\text{base}} : \max_{t_{\text{cut}} \in T_{\text{cut}}} F\left(\vec{\lambda} \mid t_{\text{cut}}\right) \geqslant f_{\text{target}} \right\}, \text{ where } \Lambda_{\text{base}} := \times_{i=1}^{m} \left[ \underline{\lambda}^{(i)}, \overline{\lambda}^{(i)} \right] , \tag{18}$$

so that no parameter is allowed to fall below its baseline. Then, the *minimality* is defined in terms of the cost function [23, 24, 34], denoted $h$, as

$$h\left(\vec{\lambda}, \vec{\underline{\lambda}}\right) := \sum_{i=1}^{m} \text{IF}\left(\lambda^{(i)}, \underline{\lambda}^{(i)}\right) , \quad \text{where} \quad \text{IF}\left(\lambda^{(i)}, \underline{\lambda}^{(i)}\right) := \frac{\ln\left(p_{\text{NI}}^{(i)}\left(\underline{\lambda}^{(i)}\right)\right)}{\ln\left(p_{\text{NI}}^{(i)}\left(\lambda^{(i)}\right)\right)} , \tag{19}$$

and the functions $p_{\text{NI}}^{(i)}$, $i \in [m]$ denote the *probability of no-imperfection*, a metric [35] that maps hardware parameters with varying ranges to $[0, 1]$. In this mapping, the functional value 1 corresponds to ideal performance such as infinite coherence time, perfect link fidelity, and 100% base efficiency; the specific forms of $p_{\text{NI}}$s are listed in table 3. Moreover, to quantify the degree of improvement required for each parameter relative to its baseline, we define the improvement factor (IF) as in (19) and define the hardware cost $h$ as the sum of the IFs across all parameters. It is important to note that the hardware cost computed through this methodology serves as a measure of the technical difficulty in enhancing hardware parameters to the specified levels, rather than representing any financial costs.

We now combine the fidelity requirement with the hardware cost to obtain the total cost for a given parameter set. This involves solving a constrained optimisation problem, where the constraint $F(\vec{\lambda} \mid t_{\text{cut}}) \geqslant f_{\text{target}}$ ensures that the target performance is met. We use scalarisation [71, 72] to convert this into an unconstrained optimisation problem, which is numerically convenient to solve. Specifically, we add the constraint as a large penalty term to $h$, yielding a new objective function $c$, which, due to the penalty term, *may* also depend on $t_{\text{cut}}$:

$$c\left(\vec{\lambda}, \vec{\underline{\lambda}}, F \mid t_{\text{cut}}\right) := \omega_1 \left(1 + \left(f_{\text{target}} - F\left(\vec{\lambda} \mid t_{\text{cut}}\right)\right)^2\right) \mathbb{1}_{F\left(\vec{\lambda} \mid t_{\text{cut}}\right) < f_{\text{target}}} + \omega_2 \, h\left(\vec{\lambda}, \vec{\underline{\lambda}}\right) . \tag{20}$$

The indicator function $\mathbb{1}_{F(\vec{\lambda}|t_{\text{cut}})<f_{\text{target}}}$ introduces a penalty when the target fidelity is not met, and the weights $\omega_1$ and $\omega_2$ control the relative importance of satisfying the constraint versus minimising hardware cost. By imposing $\omega_1 \gg \omega_2$, we ensure that the optimiser prioritises solutions satisfying $F(\vec{\lambda} \mid t_{\text{cut}}) \geqslant f_{\text{target}}$. In our implementation, we set $\omega_1 = 10^{100}$ and $\omega_2 = 1$ following [34] since the precise cost value is irrelevant when the fidelity constraint is violated. With the updated objective function $c$, the set of desired hardware parameters $\Lambda_*$ is

$$\Lambda_* := \left\{ \vec{\lambda} \in \Lambda_{\text{base}} : c\left(\vec{\lambda}, \underline{\lambda}, F \mid t_{\text{cut}}\right) = \min_{\vec{\lambda}' \in \Lambda_{\text{base}}, \tilde{t}_{\text{cut}} \in T_{\text{cut}}} c\left(\vec{\lambda}', \underline{\lambda}, F \mid \tilde{t}_{\text{cut}}\right) \right\} . \tag{21}$$

Furthermore, in conjunction with target fidelity, we can also impose a target rate $r_{\text{target}}$ with the cost function

$$\begin{aligned} c'\left(\vec{\lambda}, \underline{\lambda}, F, R \mid t_{\text{cut}}\right) :=& \omega_1 \left(1 + \left(f_{\text{target}} - F\left(\vec{\lambda} \mid t_{\text{cut}}\right)\right)^2\right) \mathbb{1}_{F\left(\vec{\lambda}|t_{\text{cut}}\right)<f_{\text{target}}} \\ &+ \omega_1' \left(1 + \left(r_{\text{target}} - R\left(\vec{\lambda} \mid t_{\text{cut}}\right)\right)^2\right) \mathbb{1}_{R\left(\vec{\lambda}|t_{\text{cut}}\right)<r_{\text{target}}} + \omega_2\, h\left(\vec{\lambda}, \underline{\lambda}\right) , \end{aligned} \tag{22}$$

and determine the optimal parameter configurations accordingly. Similar to (20), we set $\omega_1 = \omega_1' = 10^{100}$ and $\omega_2 = 1$. Finally, we solve the resulting problem using the optimisation heuristic from [73], which outputs a point $\vec{\lambda}_* \in \Lambda_*$ that is *practically* equivalent to any other point in $\Lambda_*$ considering our objective.

### 4.2. Baseline and optimistic parameter values

We take the MN parameter values from quantum communication experiments with trapped ions, a platform for which the relevant networking primitives have all been demonstrated. Empirical demonstrations of the efficacy of such systems include long-lived quantum memories [12, 74], remote entanglement generation [53–55], high-fidelity single- and two-qubit gates [75–77], and entanglement swapping [53]. Note that we do not assume that all parameters have been demonstrated in the same experimental setup.

We choose these values according to the following principle. The baseline values listed in table 3 represent either a demonstrated state-of-the-art value or a conservative estimate derived from present experimental capabilities. The optimistic values represent anticipated near-term improvements based on concrete experimental directions or theoretical projections, rather than an idealised limit. Therefore, both should be interpreted as representative benchmarks for current and near-term hardware, not as definitive bounds on future performance.

For the baseline, we observe that recent experimental work [53] has demonstrated entanglement generation over an ion–ion link with average fidelity $f_{\text{m}'}$ up to 0.88 relative to a maximally entangled state. Furthermore, coherence times ($t_{\text{coh}}$) as long as 62 ms have been achieved [12]. For the baseline base efficiency of ion–ion entanglement generation, i.e. excluding fibre loss, we take $p_{\text{m}}^0 = 5.95 \times 10^{-4}$, derived from experimental parameters in appendix A.1. Following the supplementary material of appendix [12], we take $t_{\text{prep}} = 175\,\mu\text{s}$.

To obtain the optimistic values, we incorporate anticipated near-term hardware advancements as indicated by experimental physicists at the Institute for Quantum Optics and Quantum Information, University of Innsbruck [78]. These improvements include narrowing the photon-detection coincidence window and enhancing photon detectors, which are expected to increase ion–ion link fidelity to 0.95. In addition, it is expected that employing decoherence-free subspaces [47, 79] in combination with sympathetic cooling techniques [80, 81], or using alternative ion isotopes with inherently longer coherence times [74], can extend the memory coherence time $t_{\text{coh}}$ to 4 seconds. For the base efficiency $p_{\text{m}}^0$, smaller cavities for improved ion coupling, better photon detectors, and improved frequency conversion are together expected to yield $p_{\text{m}}^0 = 1.43 \times 10^{-2}$; see derivation in appendix A.1. Note that we do not know *a priori* whether the optimistic parameter values are sufficient to satisfy our requirements. While these values are based on projections of current experimental capabilities and plausible future improvements, further improvements beyond these estimates may be possible. In this work, however, we do not consider such potential advancements and instead assess whether the optimistic parameters are adequate.

Since a backbone of length 450km has not yet been experimentally demonstrated, the corresponding baseline and optimistic values necessarily rely on model-based estimates. We therefore choose them from theoretical models of hybrid architectures that combine trapped-ion nodes with atomic ensemble-based repeaters [16, 17]. In this model, the backbone entanglement generation rate depends on the target backbone fidelity. We therefore select reference points for the baseline and optimistic parameters from the corresponding rate-fidelity trade-off curve; see Supplementary Note A [82]. During the optimisation, however, we allow $f_{\text{b}}$ and $p_{\text{b}}$ to vary independently within the region bounded by these

**Table 3.** Mapping of physical parameters to corresponding no-imperfection probabilities ($p_{\mathrm{NI}}$), which re-scale physical parameter values to the interval $[0, 1]$. Baseline values reflect the state-of-the-art values or conservative estimates based on present experimental capabilities, and optimistic values represent projected near-term improvements. We vary parameters over this range to evaluate the hardware requirements to perform teleportation. The values corresponding to the metropolitan parameters are representative of trapped-ion-based networks. For the backbone parameters, both the baseline and optimistic values are model-based estimates from [17].

| Parameter $\lambda^{(i)}$ | $p_{\mathrm{NI}}(\lambda^{(i)})$ | Baseline $\underline{\lambda}^{(i)}$ | Optimistic $\overline{\lambda}^{(i)}$ |
|---|---|---|---|
| Metropolitan base efficiency $p_{\mathrm{m}}^0$ | $p_{\mathrm{m}}^0$ | $5.95 \times 10^{-4}$ (see appendix A.1) | $1.43 \times 10^{-2}$ (see appendix A.1) |
| Coherence time $t_{\mathrm{coh}}$ | $\mathrm{e}^{-1/t_{\mathrm{coh}}}$ | 62 ms [12] | 4 s [78] |
| Metropolitan ent. fidelity $f_{\mathrm{m}}$ | $\frac{1}{3}(4f_{\mathrm{m}} - 1)$ | 0.88 [53] | 0.95 [78] |
| Backbone ent. gen. probability $p_{\mathrm{b}}$ | $p_{\mathrm{b}}$ | $1.51 \times 10^{-6}$ (see Supplementary Note A [82]) | $4.18 \times 10^{-3}$ [17] |
| Backbone ent. fidelity $f_{\mathrm{b}}$ | $\frac{1}{3}(4f_{\mathrm{b}} - 1)$ | 0.60 (see Supplementary Note A [82]) | 0.90 [17] |

two reference estimates. For the baseline, we choose the lowest backbone fidelity that, together with the baseline metropolitan link fidelity of 0.88 and in the absence of decoherence, yields an intercity teleportation fidelity of $2/3$, giving $f_{\mathrm{b}} = 0.60$. Using the formalism of [17], this corresponds to an entanglement generation rate of approximately $(1610.15\ \mathrm{s})^{-1}$ at a target fidelity of 0.60 where the hardware parameters entering the model, such as memory efficiency and number of multiplexing modes, are chosen based on the current state-of-the-art experimental values[5]. As before, we take $t_{\mathrm{prep}}$ to be $175\,\mu\mathrm{s}$ [12]. Thus, using (11) and (12), we obtain the baseline of backbone entanglement generation probability $p_{\mathrm{b}} = R_{\mathrm{b}} \times t_{\mathrm{b}} = 1.51 \times 10^{-6}$, where we used $t_{\mathrm{b}}^{\mathrm{class}} = 450/v$, and $v = 2 \times 10^5\,\mathrm{kms}^{-1}$ is the speed of light in optical fibre.

For the optimistic values, we take the target fidelity $f_{\mathrm{b}} = 0.90$ reported in [17], which yields an entanglement generation rate $R_{\mathrm{b}}$ of approximately $(0.58\ \mathrm{s})^{-1}$ and, correspondingly, an optimistic backbone entanglement generation probability $p_{\mathrm{b}} = 4.18 \times 10^{-3}$. We emphasise that although the parameter values used in our evaluations are based on quantum-networking experiments involving trapped ions and atomic ensemble-based repeaters, our modelling framework remains hardware-agnostic.

## 5. Derivation of the teleportation rate and expected fidelity in intercity network

To answer **Q2**–**Q4**, we now derive the rate and fidelity of teleportation in the IN, which are then used to obtain the hardware requirements.

### 5.1. Derivation of teleportation rate in the intercity network

In our model, the rate at which a qubit can be teleported between end nodes across the IN is determined by the time to establish an end-to-end link and the subsequent teleportation time. Let $X_{\mathrm{e2e}}$ denote the random variable representing the time to establish an end-to-end link successfully. Since data qubit preparation is instantaneous (see **A10**), the teleportation time reduces to the transmission time $t_{\mathrm{int}}^{\mathrm{class}}$ of the Pauli correction message from sender to receiver; see (14). Thus, the total time required in both ER and QR teleportation is $t_{\mathrm{int}}^{\mathrm{class}} + X_{\mathrm{e2e}}$, giving the rate

$$\text{(Teleportation rate)} \qquad R_{\mathrm{int}} = \frac{1}{\mathbb{E}\left(t_{\mathrm{int}}^{\mathrm{class}} + X_{\mathrm{e2e}}\right)} = \frac{1}{t_{\mathrm{int}}^{\mathrm{class}} + \mathbb{E}\left(X_{\mathrm{e2e}}\right)} \ . \tag{23}$$

We now focus on the derivation of $\mathbb{E}(X_{\mathrm{e2e}})$. To that end, we introduce certain notations and rephrase relevant implications from assumptions A1–**A10**.

**R1 Individual link generation times**: Recall from A9 that a cut-off time $t_{\mathrm{cut}}$ is imposed to ensure a certain quality of entanglement. We denote by $X_1$, $X_2$, and $X_{\mathrm{b}}$ the durations of *successfully* generating entanglement between $\mathrm{P}_1$ (or $\mathrm{P}_2$) and $\mathrm{B}_1$, $\mathrm{P}_3$ (or $\mathrm{P}_4$) and $\mathrm{B}_2$, and $\mathrm{B}_1$ and $\mathrm{B}_2$, respectively. We further define

$$X_{\max} := \max\{X_1, X_2, X_{\mathrm{b}}\} \ , \ X_{\min} := \min\{X_1, X_2, X_{\mathrm{b}}\} \ .$$

[5] Based on the *two-single-click protocol* of [16, 17], and values obtained using the corresponding code repository.

As explained in A9, a round succeeds if and only if all links are produced within a $t_{\text{cut}}$ time block where $t_{\text{cut}} \in T_{\text{cut}}$; see (16). Since time is discrete, we have

$$X_{\max} - X_{\min} < t_{\text{cut}} \iff X_{\max} - X_{\min} \leqslant t'_{\text{cut}} := t_{\text{cut}} - 1. \tag{24}$$

**R2 Auxiliary variables**: To denote the success of the $i$-th round, we introduce a Bernoulli random variable $Y^{(i)}$. That is, $Y^{(i)} = 1$ if end-to-end entanglement is successfully created during the $i$-th round and $Y^{(i)} = 0$ otherwise. Also, we denote by $N$ the number of rounds until success and by $Z^{(i)}$ the duration of the $i$-th round. We also assume

$$Y^{(i)} \overset{\text{IID}}{\sim} Y,\ Z^{(i)} \overset{\text{IID}}{\sim} Z, \tag{25}$$

$$\mathbb{P}(Y=1) = \mathbb{P}(X_{\max} - X_{\min} < t_{\text{cut}}) =: p\ . \tag{26}$$

Recall from A7 that entanglement swap in memory always succeeds. However, after the final swap, a classical message must reach both end nodes before the actual teleportation process can commence, which takes $t_{\text{msg}}$; see (13) and figure 2. On the other hand, for a failed round, the final link (out of three) is not generated within $t_{\text{cut}}$ since the generation of the first elementary link. At time $X_{\min}$, a classical message is sent across nodes to communicate the relevant link generation and takes a duration of at most $t_{\text{msg}}$ to reach the farthest node. Since $t_{\text{cut}} \geqslant t_{\text{msg}}$ (see (16)), all nodes can abandon ongoing link generation attempts by time $X_{\min} + t_{\text{cut}}$ and restart the round. Thus, the duration of a successful $(Y=1)$ and failed $(Y=0)$ round are

$$Z = \begin{cases} X_{\max} + t_{\text{msg}}, & \text{if } Y=1\ , \\ X_{\min} + t_{\text{cut}}, & \text{if } Y=0\ . \end{cases} \tag{27}$$

**R3 Events concerning end-to-end link generation**: We define the following events

$$A_i := \{\omega : X_{\max}(\omega) = X_i(\omega)\}\ , A_iA_j := A_i \cap A_j\ , A_1A_2A_{\text{b}} := \bigcap_{k\in\{1,2,b\}} A_k\ , i,j \in \{1,2,b\}\ . \tag{28}$$

Further, the following events correspond to $Y^{(i)} = 1$, i.e. success in the $i$-th round:

$$\begin{aligned} A_i^+ &:= \{\omega : X_{\max}(\omega) = X_i(\omega), X_{\max} - X_{\min} \leqslant t'_{\text{cut}}\}\ ; \\ A_{ij}^+ &:= \{\omega : X_{\max}(\omega) = X_i(\omega), X_{\min}(\omega) = X_j(\omega), X_{\max} - X_{\min} \leqslant t'_{\text{cut}}\}\ ; \\ A_i^+A_j^+ &:= A_i^+ \cap A_j^+\ , i,j \in \{1,2,\text{b}\}\ ; A_1^+A_2^+A_{\text{b}}^+ := \bigcap_{k\in\{1,2,\text{b}\}} A_k^+\ . \end{aligned} \tag{29}$$

For failed rounds (i.e. $Y^{(i)} = 0$), the relevant events are defined as

$$\begin{aligned} A_i^- &:= A_i - A_i^+\ , \quad i \in \{1,2,\text{b}\}\ ; \\ A_i^-A_j^- &:= A_i^- \cap A_j^-, \quad i,j \in \{1,2,\text{b}\}\ ; \\ A_{ij}^- &:= \{\omega : X_{\max}(\omega) = X_i(\omega), X_{\min}(\omega) = X_j(\omega), X_{\max} - X_{\min} \geqslant t_{\text{cut}}\}\ ; \\ A_{ij}^-A_{kl}^- &:= A_{ij}^- \cap A_{kl}^-\ , \quad i,j,k,l \in \{1,2,\text{b}\}\ . \end{aligned} \tag{30}$$

Characterisations of these events in terms of the number of attempts required to generate the metropolitan links, $M_1$ and $M_2$, and the backbone link, $M_{\text{b}}$, are given in Supplementary Note B [82].

Now R1– R3 help us derive $\mathbb{E}(X_{\text{e2e}})$, which we describe in the following theorem.

**Theorem 1.** *The expected time to successfully establish an end-to-end link is given by*

$$\mathbb{E}(X_{\text{e2e}}) = \frac{\mathbb{E}(Z\mathbb{1}_{Y=0}) + \mathbb{E}(Z\mathbb{1}_{Y=1})}{p}, \text{ where} \tag{31}$$

$$\begin{aligned} \mathbb{E}(Z\mathbb{1}_{Y=1}) = {} & 2\mathbb{E}\left(Z\mathbb{1}_{A_1^+}\right) + \mathbb{E}\left(Z\mathbb{1}_{A_{\text{b}}^+}\right) - \mathbb{E}\left(Z\mathbb{1}_{A_1^+A_2^+}\right) \\ & - 2\mathbb{E}\left(Z\mathbb{1}_{A_1^+A_{\text{b}}^+}\right) + \mathbb{E}\left(Z\mathbb{1}_{A_1^+A_2^+A_{\text{b}}^+}\right)\ , \end{aligned} \tag{32}$$

$$\begin{aligned} \mathbb{E}(Z\mathbb{1}_{Y=0}) = {} & 2\left(\mathbb{E}\left(Z\mathbb{1}_{A_{12}^-}\right) + \mathbb{E}\left(Z\mathbb{1}_{A_{1\text{b}}^-}\right) + \mathbb{E}\left(Z\mathbb{1}_{A_{\text{b}1}^-}\right)\right) \\ & - 2\mathbb{E}\left(Z\mathbb{1}_{A_{12}^-A_{1\text{b}}^-}\right) - \mathbb{E}\left(Z\mathbb{1}_{A_{\text{b}1}^-A_{\text{b}2}^-}\right) \end{aligned}$$

$$- \mathbb{E}\left(Z\mathbb{1}_{A_1^- A_2^-}\right) - 2\mathbb{E}\left(Z\mathbb{1}_{A_1^- A_b^-}\right) . \tag{33}$$

**Proof sketch** The expected end-to-end link generation time $\mathbb{E}(X_{e2e})$ is the average total duration of all rounds up to and including the first successful round. Since each round succeeds with probability $p$ (26), the number of rounds $N$ is geometrically distributed. Conditioning on $N$, the first $N-1$ rounds are failed rounds with duration distributed as $Z \mid Y=0$, while the final round is successful with duration distributed as $Z \mid Y=1$. Using linearity of expectation and the i.i.d. structure of the rounds yields (31). Finally, applying the inclusion-exclusion expansion to the corresponding events and using the symmetry of the two metropolitan links, we obtain (32) and appendix(33). See appendix C for a detailed proof. □

We calculate the individual terms of (32) and (33) in Supplementary Note B [82]. The calculation of the end-to-end entanglement generation success probability $p$ follows directly from the fidelity calculation. Hence, we present the derivation in section 5.2. In particular, $p = U_1(0)$; see (38). Plugging these in (32), (33), and (31) and subsequently in (23), we obtain the teleportation rate in the IN. Next, we derive the expressions for the expected teleportation fidelity.

### 5.2. Derivation of expected teleportation fidelity in the intercity network

In our model of ER teleportation, the fidelity of the teleported qubit depends on (i) the fidelity of the end-to-end link and (ii) the time taken to transmit the classical Pauli correction message from sender to receiver $t_{\text{int}}^{\text{class}}$; see (14). For QR teleportation, the fidelity also depends on the end-to-end link generation time, over which the data qubit decoheres. Hence, we first derive the expected fidelity of the end-to-end link in the next lemma.

**Lemma 1.** *The expected fidelity of an end-to-end entangled link in the IN is given by*

$$F_{e2e} = \frac{1 + 3\mathbb{E}(w_{e2e})}{4} , \text{ where } \quad \mathbb{E}(w_{e2e}) = \frac{w_m^2 w_b \, e^{-k t_{msg}}}{p} U_1(k) , \text{ with} \tag{34}$$

$$U_1(k) := \mathbb{E}\left(e^{-k X_{\text{diff}}} \mathbb{1}_{Y=1}\right) , \quad k := \frac{2}{t_{\text{coh}}} , \text{ and} \tag{35}$$

$$X_{\text{diff}} := \begin{cases} X_{\max} - X_{\min}, & \text{for } A_1^+ \text{and } A_2^+ , \\ 2X_b - X_1 - X_2, & \text{for } A_b^+ . \end{cases} \tag{36}$$

*Here, $w_m$ and $w_b$ are the Werner parameters of freshly generated links between an end node and its neighbouring border node, and between two border nodes across the backbone, respectively. Furthermore,*

$$\begin{aligned} U_1(v) = 2\Big(&\mathbb{E}\left(e^{-v(X_1 - X_2)}\mathbb{1}_{A_{12}^+}\right) + \mathbb{E}\left(e^{-v(X_1 - X_b)}\mathbb{1}_{A_{1b}^+}\right) - \mathbb{E}\left(e^{-v(X_1 - X_2)}\mathbb{1}_{A_{12}^+ A_{1b}^+}\right)\Big) \\ &+ \mathbb{E}\left(e^{-v(2X_b - X_1 - X_2)}\mathbb{1}_{A_b^+}\right) - \mathbb{E}\left(e^{-v(X_1 - X_b)}\mathbb{1}_{A_1^+ A_2^+}\right) \\ &- 2\mathbb{E}\left(e^{-v(X_1 - X_2)}\mathbb{1}_{A_1^+ A_b^+}\right) + \mathbb{E}\left(\mathbb{1}_{A_1^+ A_2^+ A_b^+}\right) . \end{aligned} \tag{37}$$

**Proof sketch** The expected fidelity $F_{e2e}$ is defined as the fidelity of the end-to-end link conditional on a successful end-to-end link generation, i.e. $Y=1$. The form in (34) thus follows from the definition of conditional probability. The expected end-to-end Werner parameter $\mathbb{E}(w_{e2e})$ accounts for decoherence accumulated due to the differences in the elementary link generation times before the swap. In case of $A_1^+$ and $A_2^+$, only two qubits undergo decoherence at any moment which yields $X_{\text{diff}} = X_{\max} - X_{\min}$. In contrast, for $A_b^+$, both metropolitan links wait for the backbone link such that their qubits decohere during this period, giving $X_{\text{diff}} = 2X_b - X_1 - X_2$, as in (36). Thus, for a given coherence time, $U_1(k)$ in (35) follows from (37) by the principle of inclusion-exclusion. See appendix D for the detailed proof. □

Note that the calculation of $U_1(v)$ facilitates the calculation of $p$. Specifically, we have

$$p = \mathbb{E}(\mathbb{1}_{Y=1}) = U_1(0) . \tag{38}$$

We describe the computation of $U_1(v)$ in Supplementary Note C [82] and subsequently calculate $p$, which gives the rate and fidelity via (31), (34), (39), and (40).

The fidelity of teleporting a mixed state using a Werner state as a resource is given in lemma 2. Thus, the teleportation fidelity now follows straightforwardly from lemmas 1 and 2 as described in the following two theorems.

**Theorem 2.** *The expected fidelity of a teleported qubit in the ER case is given by*

$$\text{(Expected fidelity ER)} \qquad F_{\text{int}}^{\text{ER}} = \frac{1+\mathbb{E}\left(w_{\text{e2e}}\right)\mathrm{e}^{-kt_{\text{int}}^{\text{class}}/2}}{2} = \frac{1}{2} + \frac{w_{\text{m}}^2 w_{\text{b}}\mathrm{e}^{-k\left(t_{\text{msg}}+t_{\text{int}}^{\text{class}}/2\right)}}{2p}\,U_1\left(k\right), \tag{39}$$

*where $U_1(\cdot)$ and $k$ are defined in (35), $w_{\text{m}}$ and $w_{\text{b}}$ are the Werner parameters of freshly generated links between an end node and its neighbouring border node, and between two border nodes across the backbone, respectively.*

**Proof.** In the ER scenario, only the qubit stored in the receiver node undergoes decoherence during the propagation time of the Pauli correction message between the end nodes $t_{\text{int}}^{\text{class}}$. Since the end-to-end link has Werner parameter $w_{\text{e2e}}$ (D.1), using (B.4) we obtain the expected fidelity of the teleported qubit as

$$\mathbb{E}\left(\frac{1+w_{\text{e2e}}\mathrm{e}^{-kt_{\text{int}}^{\text{class}}/2}}{2}\right) = \frac{1+\mathbb{E}\left(w_{\text{e2e}}\right)\mathrm{e}^{-kt_{\text{int}}^{\text{class}}/2}}{2} \overset{(34)}{=} \frac{1}{2} + \frac{w_{\text{m}}^2 w_{\text{b}}\mathrm{e}^{-k\left(t_{\text{msg}}+t_{\text{int}}^{\text{class}}/2\right)}}{2p}\,U_1\left(k\right),$$

which establishes (39).

□

**Theorem 3.** *The expected fidelity of a teleported qubit in the QR case is given by*

$$\text{(Expected fidelity QR)} \quad F_{\text{int}}^{\text{QR}} = \frac{1}{2} + \frac{1}{2}w_{\text{m}}^2 w_{\text{b}}\mathrm{e}^{-k\left(3t_{\text{msg}}+t_{\text{int}}^{\text{class}}\right)/2}\frac{U_2\left(k\right)}{1-\mathrm{e}^{-kt_{\text{cut}}/2}\,U_3\left(k\right)}, \text{ where} \tag{40}$$

$$U_2\left(v\right) := \mathbb{E}\left(\mathrm{e}^{-v\left(X_{\text{diff}}+X_{\max}/2\right)}\mathbb{1}_{Y=1}\right), \quad k = \frac{2}{t_{\text{coh}}}, \tag{41}$$

$$U_3\left(v\right) := \mathbb{E}\left(\mathrm{e}^{-vX_{\min}/2}\mathbb{1}_{Y=0}\right). \tag{42}$$

*Here, $t_{\text{coh}}$ is the memory coherence time of an end or border node, $w_{\text{m}}$ and $w_{\text{b}}$ are the Werner parameters of freshly generated links between an end node and its neighbouring border node, and between two border nodes across the backbone, respectively. Furthermore,*

$$\begin{aligned} U_2\left(v\right) = {} & 2\left(\mathbb{E}\left(\mathrm{e}^{-v\left(3X_1/2-X_2\right)}\mathbb{1}_{A_{12}^+}\right)+\mathbb{E}\left(\mathrm{e}^{-v\left(3X_1/2-X_{\text{b}}\right)}\mathbb{1}_{A_{1\text{b}}^+}\right)-\mathbb{E}\left(\mathrm{e}^{-v\left(3X_1/2-X_2\right)}\mathbb{1}_{A_{12}^+A_{1\text{b}}^+}\right)\right) \\ & +\mathbb{E}\left(\mathrm{e}^{-v\left(5X_{\text{b}}/2-X_1-X_2\right)}\mathbb{1}_{A_{\text{b}}^+}\right)-\mathbb{E}\left(\mathrm{e}^{-v\left(3X_1/2-X_{\text{b}}\right)}\mathbb{1}_{A_1^+A_2^+}\right)-2\mathbb{E}\left(\mathrm{e}^{-v\left(3X_1/2-X_2\right)}\mathbb{1}_{A_1^+A_{\text{b}}^+}\right) \\ & +\mathbb{E}\left(\mathrm{e}^{-vX_1/2}\mathbb{1}_{A_1^+A_2^+A_{\text{b}}^+}\right), \end{aligned} \tag{43}$$

$$\begin{aligned} U_3\left(v\right) = {} & 2\left(\mathbb{E}\left(\mathrm{e}^{-vX_2/2}\mathbb{1}_{A_{12}^-}\right)+\mathbb{E}\left(\mathrm{e}^{-vX_{\text{b}}/2}\mathbb{1}_{A_{1\text{b}}^-}\right)-\mathbb{E}\left(\mathrm{e}^{-vX_2/2}\mathbb{1}_{A_{12}^-A_{1\text{b}}^-}\right)\right) \\ & +2\mathbb{E}\left(\mathrm{e}^{-vX_1/2}\mathbb{1}_{A_{\text{b}1}^-}\right)-\mathbb{E}\left(\mathrm{e}^{-vX_1/2}\mathbb{1}_{A_{\text{b}1}^-A_{\text{b}2}^-}\right) \\ & -\mathbb{E}\left(\mathrm{e}^{-vX_{\text{b}}/2}\mathbb{1}_{A_1^-A_2^-}\right)-2\mathbb{E}\left(\mathrm{e}^{-vX_2/2}\mathbb{1}_{A_1^-A_{\text{b}}^-}\right). \end{aligned} \tag{44}$$

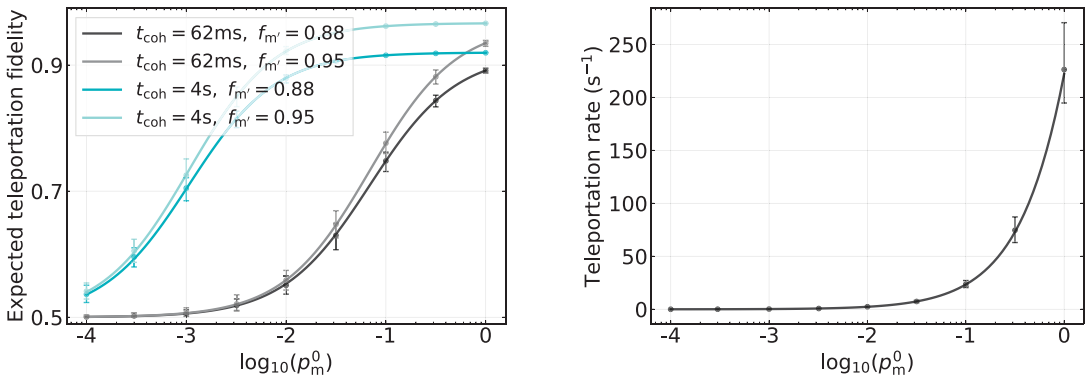
**Proof sketch** In QR teleportation, the expected fidelity $F_{\text{int}}^{\text{QR}}$ is defined as the fidelity of the teleported qubit conditional on a successful end-to-end link generation, i.e. $Y=1$, after teleportation. Since the data qubit is prepared before end-to-end link generation begins, it decoheres over the $N-1$ failed rounds, which are i.i.d. and during the final ($N^{\text{th}}$) successful round. After the BSM on the sender's qubits, the receiver's qubit additionally decoheres during the classical message propagation time $t_{\text{int}}^{\text{class}}$. Combining these terms with the end-to-end Werner parameter $w_{\text{e2e}}$ from (D.1), and using (B.4) we obtain the expected fidelity of the teleported qubit as in (40). Thus, for a given coherence time, $U_2(k)$ (41) and $U_3(k)$ (42) are calculated using the principle of inclusion-exclusion as in (43) and (44), respectively. See appendix E for a detailed proof. □

Observe that instead of evaluating $U_1(v)$ and $U_2(v)$ separately, we can compute

$$\begin{aligned} U\left(v,\alpha\right) = {} & 2\left(\mathbb{E}\left(\mathrm{e}^{-v\left((\alpha-1)X_1-X_2\right)}\mathbb{1}_{A_{12}^+}\right)+\mathbb{E}\left(\mathrm{e}^{-v\left((\alpha-1)X_1-X_{\text{b}}\right)}\mathbb{1}_{A_{1\text{b}}^+}\right)-\mathbb{E}\left(\mathrm{e}^{-v\left((\alpha-1)X_1-X_2\right)}\mathbb{1}_{A_{12}^+A_{1\text{b}}^+}\right)\right) \\ & +\mathbb{E}\left(\mathrm{e}^{-v\left(\alpha X_{\text{b}}-X_1-X_2\right)}\mathbb{1}_{A_{\text{b}}^+}\right)-\mathbb{E}\left(\mathrm{e}^{-v\left((\alpha-1)X_1-X_{\text{b}}\right)}\mathbb{1}_{A_1^+A_2^+}\right)-2\mathbb{E}\left(\mathrm{e}^{-v\left((\alpha-1)X_1-X_2\right)}\mathbb{1}_{A_1^+A_{\text{b}}^+}\right) \\ & +\mathbb{E}\left(\mathrm{e}^{-v(\alpha-2)X_1}\mathbb{1}_{A_1^+A_2^+A_{\text{b}}^+}\right), \end{aligned} \tag{45}$$

which gives

$$U_1\left(v\right) = U\left(v,2\right), \quad U_2\left(v\right) = U\left(v,5/2\right). \tag{46}$$




(a) Expected teleportation fidelity (b) Teleportation rate

**Figure 3.** Comparison of analytical (lines) and simulation results (dots) for qubit-ready teleportation in an MN. The mean, along with the 5th and 95th percentiles of the performance metrics, is shown as a function of the base efficiency $p_m^0$. (a) The expected teleportation fidelity is evaluated for both baseline and optimistic values of memory coherence time $t_{coh}$ and metropolitan link fidelity $f_{m'}$, while (b) the teleportation rate depends solely on $p_m^0$. Simulation results closely match the analytical values.

We evaluate the individual terms of (45), and those of $U_3$ in (44), in Supplementary Note C [82]. Substituting them in (45) gives $U_1$ and $U_2$ via (46), which gives the ER fidelity via (39), and together with $U_3$, the QR fidelity via (40). These expressions let us analyse the performance metrics as functions of the hardware parameters without running extensive simulations, which we take up in the next section.

## 6. Evaluations

In this section, we determine the empirical requirements corresponding to **Q1**–**Q4** for the network in figure 1, using the baseline and optimistic parameters in table 3. As already mentioned, these questions involve the teleportation rate and fidelity, which we derive analytically. This lets us answer the questions without having to run extensive simulations. We first provide empirical validation of our analytical results and then present the requirements for teleportation in the MN and IN separately. We emphasise that the validation establishes the correctness of the analytical expressions under the specified assumptions; it does not test the assumptions themselves.

### 6.1. Teleportation in a metropolitan network

Recall that in **Q1**, we consider teleportation between end nodes separated by 50 km in an MN of figure 1. The key hardware parameters that influence the performance metrics, i.e. the expected teleportation fidelity and rate, are the base efficiency $p_m^0$, memory coherence time $t_{coh}$, and metropolitan link fidelity $f_{m'}$. We explain in appendix A.3 that the teleportation fidelity in the ER case is deterministic, while the rate equals that of the QR case (see appendix A.2). Thus, we compare the analytically derived expected teleportation fidelity and rate with their empirical values only in the QR case. The empirical values are obtained by simulation in NetSquid using the code [83], and we present the comparison in figure 3.

To simulate average fidelities, we fix $t_{coh}$ and $f_{m'}$ at their baseline and optimistic values, $(62\,\text{ms}, 4\,\text{s})$ and $(0.88, 0.95)$, respectively, while varying $p_m^0$ between $10^{-4}$ and 1, keeping $t_{prep} = 175\,\mu\text{s}$, following the supplementary material of [12]. For each observation point, we run the simulation for 100 batches, with each batch comprising 100 independent runs. Each batch produces a single observation for the average teleportation fidelity and rate, from which we compute the mean and the 5th and 95th percentiles. Further, the analytical values of the expected fidelity are derived using (A.7). We observe close agreement between the analytical and simulation results in figure 3(a). Since the teleportation rate depends only on $p_m^0$, we calculate the simulated rate for each batch as a function of $p_m^0$ and the analytical value using (A.3). We observe in figure 3(b) that the analytical and simulation results are consistent in this case as well.

We now address **Q1**, i.e. identify the hardware requirements necessary to attain teleportation in the MN with target fidelity 2/3. As mentioned, the baseline hardware parameter values are set as per table 3. Since the hardware parameter space is three-dimensional, within this space we plot the surface

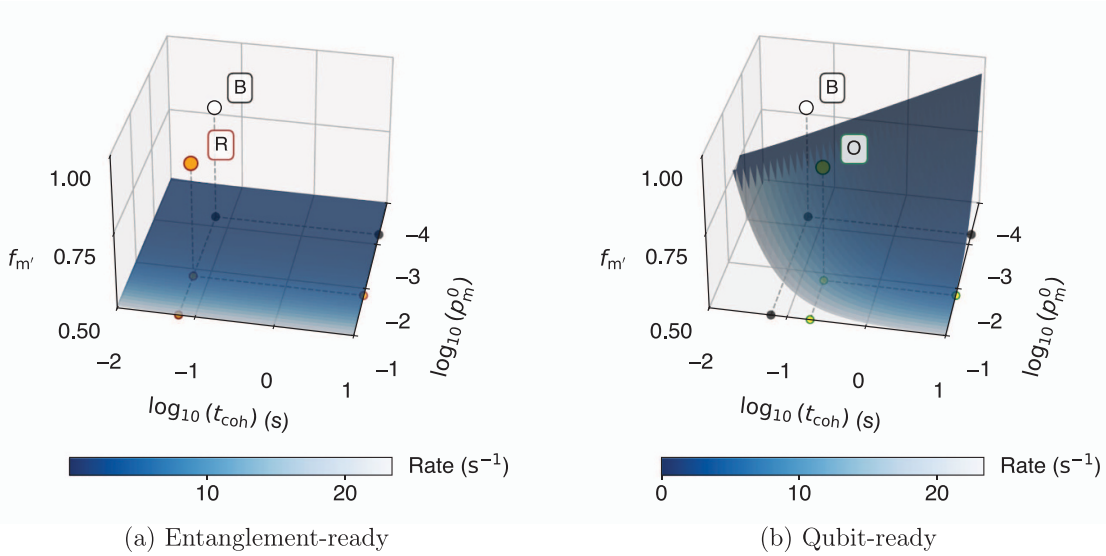



**Figure 4.** Requirements to achieve the target teleportation fidelity of 2/3 in an MN. The surfaces represent the minimum required metropolitan link fidelity $f_{m'}$ as a function of $p_m^0$ and $t_{coh}$ for (a) entanglement-ready and (b) qubit-ready teleportation. The colour of the surface shows the corresponding teleportation rate. The baseline (denoted (B) in (a) already achieves the target fidelity, while an optimal (denoted (O) parameter configuration subject to hardware cost $c$ is shown in (b). The configuration denoted by R in (a) achieves the same rate as O in (b). The $(p_m^0, t_{coh}, f_{m'})$ coordinates of the points are B: $(5.95 \times 10^{-4}, 62\,\text{ms}, 0.88)$, O: $(1.43 \times 10^{-2}, 196\,\text{ms}, 0.88)$, and R: $(1.43 \times 10^{-2}, 62\,\text{ms}, 0.88)$.

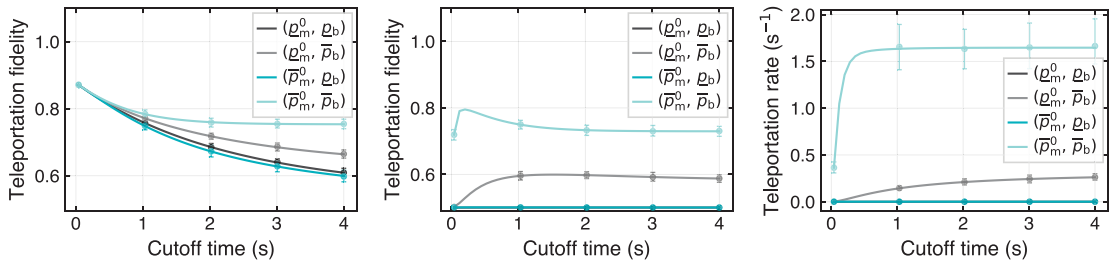
corresponding to the minimum link fidelity $f_{m'}$ required to achieve the target fidelity. For ER teleportation, we plot the surface in figure 4(a), whose colour represents the corresponding teleportation rate. As expected, the rate depends only on the base efficiency $p_m^0$. We observe that the baseline $(p_m^0, t_{coh}, f_{m'})$ denoted by B: $(5.95 \times 10^{-4}, 62\,\text{ms}, 0.88)$, lies above the surface, implying that state-of-the-art hardware already reaches the classical limit for ER teleportation in the MN. Specifically, the baseline yields an expected teleportation fidelity of 0.92 at a rate of $0.14\,s^{-1}$.

For QR teleportation, we show the surface in figure 4(b), where the colour again indicates the corresponding rate. In contrast to figure 4(a), the baseline (B) in this case lies below the surface, indicating that the current hardware capabilities cannot meet the target fidelity. Thus, we numerically identify an optimal point, corresponding to a hardware parameter configuration, that meets the target while requiring the smallest improvement over the baseline, as measured by the cost function $c$ from (20), using a global optimisation heuristic from [73]. For improved accuracy, we run the optimiser 50 times and select the solution with the lowest hardware cost among all runs. The resulting optimal point O: $(1.43 \times 10^{-2}, 196\,\text{ms}, 0.88)$ is shown in figure 4(b), which yields the target fidelity 2/3 at a rate of $3.36\,s^{-1}$. Since these analyses only constrain the fidelity, the resulting rates for the ER case and QR optimum are substantially different. To identify an ER configuration that achieves both the target fidelity and the same rate as the QR optimum O, we include the penalty term associated with the target rate in the total cost (22). The resulting optimal point, R: $(1.43 \times 10^{-2}, 62\,\text{ms}, 0.88)$, is shown in orange in figure 4(a). As expected, the hardware requirements are less stringent in the ER case than in the QR case.

### 6.2. Teleportation in intercity network

As discussed in **Q2**–**Q4**, we investigate teleportation across 500 km in the IN of figure 1. Here, each end node is located 25 km from its respective hub, and the hubs are connected by a 450 km backbone. The key hardware parameters influencing the teleportation fidelity and rate include the metropolitan base efficiency $p_m^0$, memory coherence time $t_{coh}$, metropolitan link fidelity $f_m$, entanglement generation probability in the backbone $p_b$, and backbone fidelity $f_b$, together with the non-hardware parameter cut-off time $t_{cut}$. Similar to section 6.1, we rely on analytical expressions for the teleportation rate (theorem 1 and (23)) and expected fidelity (theorems 2 and 3) to answer **Q2**–**Q4** as this obviates the need to run extensive simulations. We also validate the analytical results against corresponding empirical estimates from NetSquid-based simulations [83].

For validation, we fix $p_m^0$ and $p_b$ at their baseline and optimistic values, $(5.95 \times 10^{-4}, 1.43 \times 10^{-2})$ and $(1.51 \times 10^{-6}, 4.18 \times 10^{-3})$, respectively, while varying $t_{cut}$ between 0.04 s and 4 s. Note that the other parameters, namely, $t_{coh}$, $f_m$, and $f_b$, are kept at their optimistic values, 4 s, 0.95, and 0.9, respectively.




(a) Entanglement-ready fidelity (b) Qubit-ready fidelity (c) Teleportation rate

**Figure 5.** Comparison of analytical (lines) and simulation results (dots) as a function of cut-off time $t_{\text{cut}}$. Panels (a) and (b) show the expected teleportation fidelity for entanglement-ready and qubit-ready teleportation, respectively, while panel (c) shows the teleportation rate. Each simulation point corresponds to the mean of batch averages, with error bars denoting the 5th and 95th percentiles across batch averages. The entanglement generation probabilities $p_{\text{m}}^0$ and $p_{\text{b}}$ are set to their baseline ($\underline{p}_{\text{m}}^0 = 5.95 \times 10^{-4}, \underline{p}_{\text{b}} = 1.51 \times 10^{-6}$) and optimistic values ($\overline{p}_{\text{m}}^0 = 1.43 \times 10^{-2}, \overline{p}_{\text{b}} = 4.18 \times 10^{-3}$), as indicated in the legend. All remaining parameters are fixed at their respective optimistic values, i.e. $\bar{f}_{\text{m}} = 0.95$, $\bar{t}_{\text{coh}} = 4\,\text{s}$, and $\bar{f}_{\text{b}} = 0.90$. The analytical results match closely with the empirical estimates.

Similar to section 6.1, we obtain the empirical estimates (mean and percentiles) from simulation. We provide the comparison for the ER and QR cases in figures 5(a) and 5(b), respectively. Since the rate is the same for both cases, we do not make any distinction. The corresponding comparison is shown in figure 5(c). The close agreement between analytical and simulation results confirms the accuracy of our analytical results.

The ER fidelity (figure 5(a)) decreases monotonically with the cut-off time, since longer cut-offs allow noisier elementary links to contribute, degrading the overall end-to-end fidelity. In contrast, the QR fidelity (figure 5(b)) is non-monotonic; here, short cut-off times frequently discard noisy links, leading to prolonged end-to-end link generation times and causing increased decoherence for the data qubit. Although this improves the fidelity of the end-to-end link, the overall teleportation fidelity suffers due to data qubit degradation. For larger cut-off times, the average waiting time decreases, but we allow elementary links with lower fidelity to form the end-to-end link. This naturally leads to the formation of a low-fidelity end-to-end link and, subsequently, low teleportation fidelity. In contrast, we observe from figure 5(c) that the teleportation rate, which is the inverse of the expected end-to-end link generation time, always increases with $t_{\text{cut}}$, as expected. Therefore, figure 5(b) shows that, for a given parameter set, the same teleportation fidelity can be achieved for two different $t_{\text{cut}}$; since the rate increases monotonically with $t_{\text{cut}}$, we report the higher of the two rates at each point where the target fidelity is met in the following figures.

Recall that in **Q2**, we aim to find the minimal metropolitan requirements to reach the target teleportation fidelity $2/3$ while the backbone parameters are fixed at their optimistic values: $\overline{p}_{\text{b}} = 4.18 \times 10^{-3}, \bar{f}_{\text{b}} = 0.90$; see table 3. Similar to figure 4(a), we plot the surface in figure 6(a), representing the minimum required metropolitan link fidelity $f_{\text{m}}$ needed to achieve the target ER fidelity. The region above this surface corresponds to the desired parameter space that achieves fidelity higher than $2/3$. The colour of the surface in figure 6(a) represents the achievable teleportation rate corresponding to the points on the surface. We observe that for a fixed $t_{\text{coh}}$, the required $f_{\text{m}}$ does not change much with $p_{\text{m}}^0$, but for $t_{\text{coh}} \leqslant 0.02\,\text{s}$, the required $f_{\text{m}}$ increases sharply and the target eventually becomes unachievable. Moreover, since we vary $t_{\text{cut}}$ in the range (16), the rate is implicitly influenced by $t_{\text{coh}}$ via $t_{\text{cut}}$. As a result, for a fixed $p_{\text{m}}^0$, increasing $t_{\text{coh}}$ allows for longer cut-off times, leading to higher rates. Also, as expected, the rate increases monotonically with $p_{\text{m}}^0$, most visibly at large $t_{\text{coh}}$ and $p_{\text{m}}^0$. A crucial observation from figure 6(a) is that the baseline B: $(5.95 \times 10^{-4}, 62\,\text{ms}, 0.88)$ (shown in white) lies above the surface, indicating that we can already reach the target fidelity of $2/3$ in the ER case under state-of-the-art metropolitan hardware and optimistic backbone parameters. The maximum rate achievable in this configuration is $4.00 \times 10^{-4}\,\text{s}^{-1}$ at the target fidelity.

Analogously, we plot the corresponding surface for the QR scenario in figure 6(b), where the colour denotes the *maximum* achievable teleportation rate. Here, the baseline point B (shown in white) falls below the surface. Hence, we optimise as in section 6.1, and obtain the optimal point O: $(1.40 \times 10^{-2}, 1095\,\text{ms}, 0.94)$ as shown in yellow in figure 6(b), which yields the target fidelity at a rate of $1.32\,\text{s}^{-1}$. To identify an ER configuration that achieves both the target fidelity and the same rate as the QR optimum, we use the total cost (22) and obtain R: $(1.36 \times 10^{-2}, 359\,\text{ms}, 0.93)$, as shown in orange in figure 6(a).

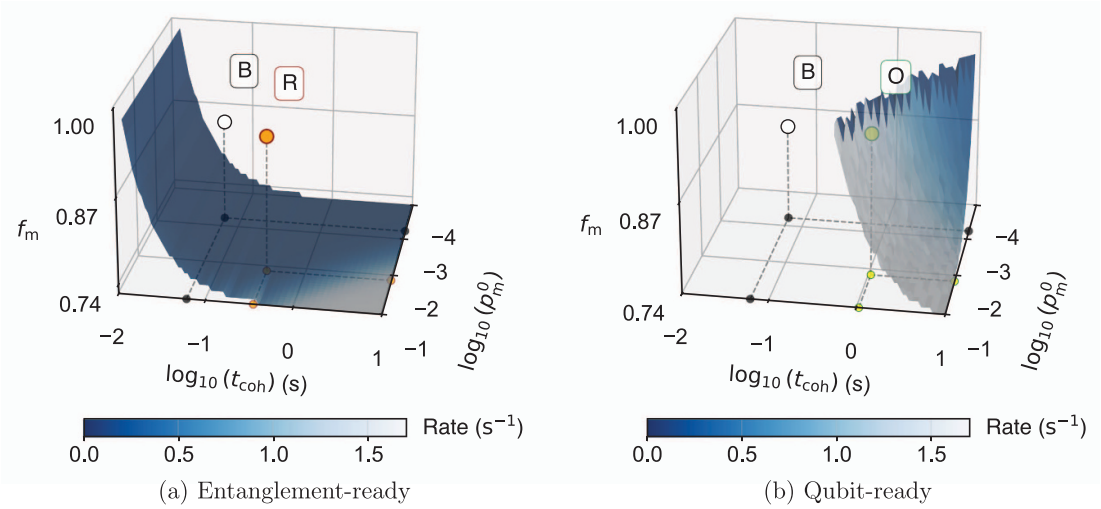



**Figure 6.** Requirements to achieve the target teleportation fidelity of 2/3 in an IN with the backbone parameters fixed at optimistic values: $\bar{p}_b = 4.18 \times 10^{-3}, \bar{f}_b = 0.9$. The surface represents the minimum required link fidelity $f_m$ as a function of the base efficiency $p_m^0$ and the memory coherence time $t_{coh}$ for (a) entanglement-ready and (b) qubit-ready teleportation. The colour of the surface encodes the maximum achievable teleportation rate, subject to meeting the target teleportation fidelity. The baseline (denoted B) in (a) already achieves the target teleportation fidelity, while an optimal (denoted O) parameter configuration subject to minimising the hardware cost $c$ is shown in (b). The configuration denoted by R in (a) achieves the same rate as O in (b). The $(p_m^0, t_{coh}, f_m)$ coordinates of the points are B: $(5.95 \times 10^{-4}, 62\,\text{ms}, 0.88)$, O: $(1.40 \times 10^{-2}, 1095\,\text{ms}, 0.94)$, and R: $(1.36 \times 10^{-2}, 359\,\text{ms}, 0.93)$.

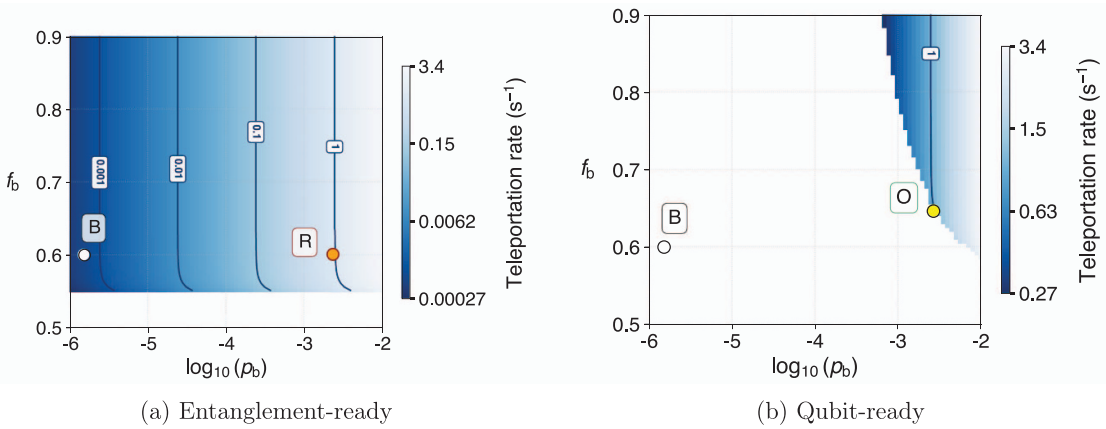



**Figure 7.** Requirements to achieve the target teleportation fidelity of 2/3 in an IN where the metropolitan parameters are fixed at their respective optimistic values $\bar{p}_m^0 = 1.43 \times 10^{-2}, \bar{t}_{coh} = 4\,\text{s}, \bar{f}_m = 0.95$. The coloured region represents the parameter space for which the teleportation fidelity is greater than or equal to 2/3 in the entanglement-ready (a) and qubit-ready (b) cases, respectively, and the colour encodes the maximum achievable teleportation rate. The baseline (denoted (B) in (a) already achieves the target teleportation fidelity, while the optimal (denoted (O) parameter configuration subject to hardware cost $c$ is shown in (b). The configuration denoted by R in (a) achieves the same rate as O in (b). The $(p_b, f_b)$ coordinates of the points are B: $(1.51 \times 10^{-6}, 0.60)$, O: $(2.73 \times 10^{-3}, 0.64)$, and R: $(2.35 \times 10^{-3}, 0.60)$. The contour lines indicate parameter combinations that yield equal rates.

We now address **Q3**, where we fix the metropolitan parameters at their respective optimistic values $\bar{p}_m^0 = 1.43 \times 10^{-2}, \bar{t}_{coh} = 4\,\text{s}, \bar{f}_m = 0.95$ (see table 3) and identify the backbone requirements. Since the backbone parameter space is two-dimensional, spanned by the entanglement generation probability $p_b$ and link fidelity $f_b$, we plot the desired parameter space in figure 7(a) that achieves the target teleportation fidelity. Here, the colour represents the corresponding achievable teleportation rate, and the contour lines indicate the parameter combinations that yield equal rates in units of $s^{-1}$. For a fixed $p_b$, a lower $f_b$ requires a shorter cut-off to meet the target fidelity and therefore yields a lower rate. As $f_b$ increases, the configuration achieves the target fidelity with a much higher cut-off, leading to a higher rate. However, beyond a certain threshold, further increasing $f_b$ offers no additional benefit, as the rate becomes limited by $p_b$ within the allowed cut-off range (16). This effect is reflected in the shape of the contours, which are curved at low $f_b$ and become vertical as $f_b$ increases. Furthermore, the backbone baseline $(p_b, f_b)$,

denoted by B: $(1.51 \times 10^{-6}, 0.60)$, lies within the desired space, achieving the target fidelity at a maximum rate of $6.16 \times 10^{-4}\,\mathrm{s}^{-1}$.

For the QR case, we similarly plot the desired space in figure 7(b), where the colour again represents the *maximum* achievable rate. In contrast to the ER case, the baseline B lies outside the desired region, and we therefore numerically optimise over the backbone parameter space. Using a similar optimisation procedure as before, we obtain the optimal point O: $(2.73 \times 10^{-3}, 0.64)$ shown in yellow in figure 7(b), which achieves an expected fidelity of $2/3$ at a maximum rate of $0.92\,\mathrm{s}^{-1}$. Furthermore, in the ER scenario, the optimal point that achieves the same rate and fidelity as the QR optimum is R: $(2.35 \times 10^{-3}, 0.60)$, shown in orange in figure 7(a). As expected, the hardware requirements are less stringent for ER teleportation than in the QR case.

Finally, in **Q4**, we aim to determine the minimal hardware improvements over the baseline values of both metropolitan and backbone parameters necessary to reach the target teleportation fidelity. In this setting, all five hardware parameters, namely the metropolitan base efficiency $p_{\mathrm{m}}^0$, memory coherence time $t_{\mathrm{coh}}$, metropolitan link fidelity $f_{\mathrm{m}}$, backbone entanglement generation probability $p_{\mathrm{b}}$, and backbone link fidelity $f_{\mathrm{b}}$ are allowed to vary, alongside the cut-off time $t_{\mathrm{cut}}$. Using the baseline values, the maximum achievable expected teleportation fidelities are 0.61 and 0.50 in the ER and QR cases, respectively, both below threshold. This indicates that hardware improvements are necessary in both cases. Due to the high dimensionality of the parameter space, we do not visualise the full desired space and optimisation landscape. Instead, we numerically identify an optimal parameter configuration with the minimal hardware cost, using a method similar to section 6.1. For the ER case, the $(p_{\mathrm{m}}^0, t_{\mathrm{coh}}, f_{\mathrm{m}}, p_{\mathrm{b}}, f_{\mathrm{b}})$ coordinates of the resulting optimal point are $(6.45 \times 10^{-4}, 64\,\mathrm{ms}, 0.89, 1.57 \times 10^{-6}, 0.67)$, which reaches the target teleportation fidelity of $2/3$ at a rate of $2.58 \times 10^{-9}\,\mathrm{s}^{-1}$. Note that $f_{\mathrm{b}}$ stands out as the dominant bottleneck, while improvements in the other parameters remain modest. In the QR case, the coordinates of the corresponding optimal point are $(1.41 \times 10^{-2}, 1128\,\mathrm{ms}, 0.95, 4.16 \times 10^{-3}, 0.87)$, which reaches teleportation fidelity of $2/3$ at a *maximum* rate of $1.24\,\mathrm{s}^{-1}$. Since the optimal point in the ER case yields an impractically low rate, we additionally determine the parameter configuration that simultaneously achieves both the target fidelity and the rate attained at the QR optimum, obtaining $(1.42 \times 10^{-2}, 472\,\mathrm{ms}, 0.91, 4.13 \times 10^{-3}, 0.82)$. As expected, the improvements are significantly more demanding than in the ER case without a target rate, with $p_{\mathrm{m}}^0$, $t_{\mathrm{coh}}$, and $p_{\mathrm{b}}$ requiring substantial enhancement.

So far we have taken the classical limit $2/3$ as the target fidelity. However, with all parameters set to their optimistic values, the highest attainable teleportation fidelity in the IN is 0.87 in the ER case. To assess how the requirements depend on the choice of target fidelity, we repeat the analysis for questions similar to **Q1**–**Q4** for a higher target fidelity of 0.77, the midpoint between $2/3$ and 0.87. Here, three observations follow. First, ER teleportation no longer reaches the target when parameters assume baseline values for **Q2** and **Q3**. The optimal $(p_{\mathrm{m}}^0, t_{\mathrm{coh}}, f_{\mathrm{m}})$ coordinates for the MN are $(6.35 \times 10^{-4}, 63\,\mathrm{ms}, 0.90)$ and the optimal $(p_{\mathrm{b}}, f_{\mathrm{b}})$ coordinates for the backbone are $(2.55 \times 10^{-6}, 0.73)$, so that the required improvements remain modest in terms of hardware cost and primarily involve improvement in link fidelities. In the QR case, the corresponding optima are $(1.42 \times 10^{-2}, 2990\,\mathrm{ms}, 0.95)$ and $(3.99 \times 10^{-3}, 0.85)$, respectively. Second, the QR requirements are stricter throughout; for **Q4**, the optimal $(p_{\mathrm{m}}^0, t_{\mathrm{coh}}, f_{\mathrm{m}}, p_{\mathrm{b}}, f_{\mathrm{b}})$ moves from $(1.41 \times 10^{-2}, 1128\,\mathrm{ms}, 0.95, 4.16 \times 10^{-3}, 0.87)$ at target fidelity $2/3$ to $(1.40 \times 10^{-2}, 3290\,\mathrm{ms}, 0.95, 4.15 \times 10^{-3}, 0.90)$ at target fidelity 0.77 with a maximum rate of $1.48\,\mathrm{s}^{-1}$. Thus, the higher target fidelity mainly increases the required coherence time and backbone fidelity, bringing the latter close to its optimistic value, while the link generation probabilities and metropolitan link fidelity remain essentially unchanged near their optimistic values. Note that the maximum achievable rate at the optimum increases from $1.24\,\mathrm{s}^{-1}$ to $1.48\,\mathrm{s}^{-1}$ despite the stricter target fidelity. This is because the larger required coherence time widens the admissible range of cut-off times (16), and the rate increases monotonically with $t_{\mathrm{cut}}$; see figure 5(c). Third, the higher target fidelity remains attainable within the optimistic parameter ranges, even in the QR case. However, compared to the case with the target fidelity of $2/3$, it requires significantly larger improvements in $t_{\mathrm{coh}}$ and $f_{\mathrm{b}}$.

In figure 8, we show the IFs of the optimal configurations for both targets, with the legends indicating ER or QR cases of relevant questions. The length of each bar is normalised relative to the IF associated with the optimistic value of the corresponding parameter, shown in solid black. Annotations next to the bars indicate the actual IFs determined by the optimisation procedure. Recall from (19) that the baseline of a parameter corresponds to the IF of 1. Along the vertical axis, we represent different hardware parameters. Here $f_{(\cdot)}$ refers to $f_{\mathrm{m}'}$ for Q1-QR, and $f_{\mathrm{m}}$ elsewhere. We represented $f_{\mathrm{m}'}$ and $f_{\mathrm{m}}$ together, as they share the same baseline and the same optimistic values. Note that across all instances of QR teleportation, and at both targets, the optimal metropolitan base efficiency $p_{\mathrm{m}}^0$ is driven to its optimistic value, since its available room for improvement in terms of IF is low compared to other parameters. In Q1-QR at the target fidelity of $2/3$, for instance, metropolitan link fidelity $f_{\mathrm{m}'}$ remains near

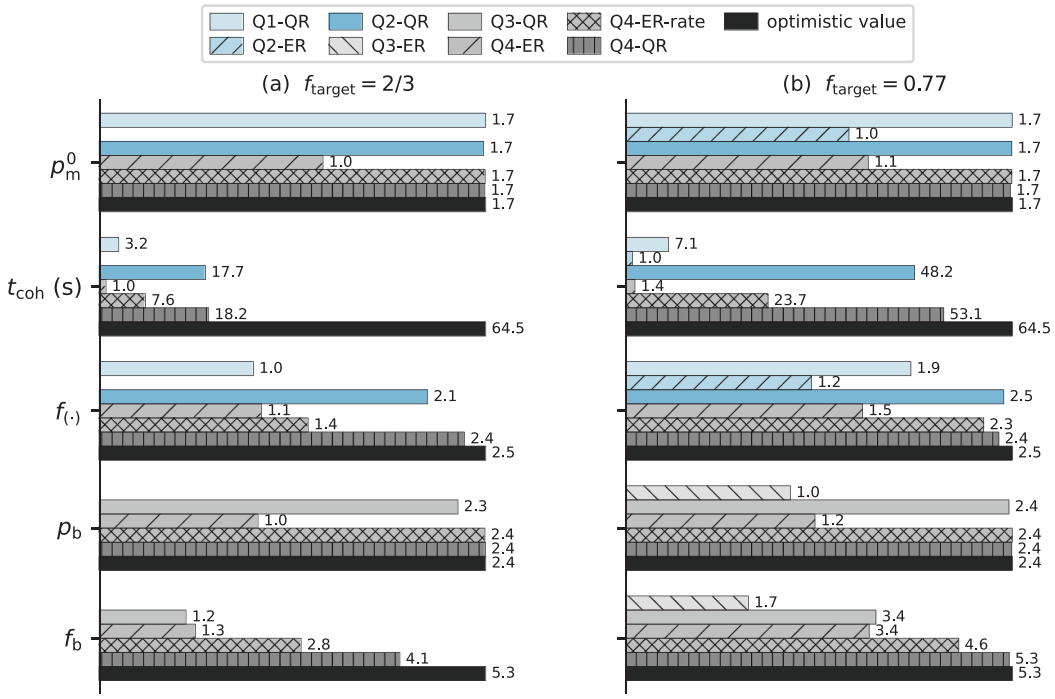



**Figure 8.** Required improvements in individual hardware parameters to reach the teleportation fidelity in **Q1**–**Q4**, with a target of 2/3 (a) and 0.77 (b). Improvement factors quantify the extent to which a given parameter must be enhanced relative to its baseline value to meet the target. A factor of 1 indicates no required improvement, while larger values reflect increasingly stringent requirements. The length of each bar represents the improvement factor normalised relative to the corresponding optimistic value, shown in black. Annotations beside the bars indicate the actual improvement factors for the relevant question. Here $f_{(\cdot)}$ refers to $f_{m'}$ for **Q1**-QR and $f_m$ in all other cases. We represent the two together as they share the same baseline and the same optimistic values. Note that not all hardware parameters are relevant for every question considered. Furthermore, in (a), **Q2**-ER and **Q3**-ER already reach the target fidelity at baseline, so no improvement is required, and the corresponding bars are omitted in the plot.

its baseline, i.e. corresponding to an IF of 1, indicating that enhancing $p_m^0$ and $t_{coh}$ is relatively more beneficial from a cost-performance perspective. In contrast, for more demanding scenarios such as **Q2**-QR and **Q4**-QR, $f_m$ is pushed close to its optimistic value while $t_{coh}$ is moderately improved, suggesting $f_m$'s effectiveness over $t_{coh}$ from the perspective of cost-performance trade-off. Regarding the backbone parameters, **Q3**-QR at the target fidelity of 2/3 calls for a substantial improvement in the backbone link generation probability $p_b$, compared to the corresponding link fidelity $f_b$, again reflecting the cost-performance trade-off. In **Q4**-ER, all parameters require only modest improvements from their baselines, except for $f_b$, which stands out as the key bottleneck. In contrast, **Q4**-QR demands near-optimistic improvements in $p_m^0$, $f_m$, and $p_b$, with moderate improvements in $t_{coh}$ and $f_b$, indicating that enhancing $p_m^0$, $f_m$, and $p_b$ is more efficient under the considered cost function. Comparing the two panels, we observe that the preference for the link generation probabilities is unchanged at the higher target fidelity. However, the relative weight of the backbone parameters does shift; for Q3-QR in figure 8(b), the IF of $f_b$ grows from 1.2 to 3.4, overtaking that of $p_b$, which rises only from 2.3 to 2.4, since it is already close to its optimistic value. Backbone fidelity therefore becomes the limiting parameter once the target fidelity is raised well above the classical limit.

From an experimental perspective, the requirements can be interpreted as follows. For the metropolitan trapped-ion links under the double-click protocol, increasing $p_m^0$ corresponds to improving the overall ion-photon entanglement generation efficiency through better photon collection, stronger ion-cavity coupling, improved fibre coupling, higher detector efficiencies, and more efficient frequency conversion. Improving $f_{m'}$ corresponds to reducing imperfections such as imperfect photon interference, detector noise, and state preparation and measurement errors. Increasing $t_{coh}$ corresponds to extending the memory lifetime, for instance through decoherence-free subspace encoding, sympathetic cooling, or alternative ion species with longer coherence times. For the backbone, improving $p_b$ and $f_b$ corresponds to increasing the effective entanglement generation probability and fidelity of the state produced by the repeater chain. For a repeater chain composed of ensemble-based memories and SPDC photon pair sources using a single-click protocol, the same hardware improvement can affect both the rate and fidelity. Such improvements correspond to higher memory efficiency, improved multiplexing, improved

photon-pair generation and collection, reduced retrieval loss, and improved SPDC photon generation efficiency.

## 7. Conclusion and future work

In this work, we present an analysis to identify the hardware requirements for enabling quantum teleportation over metropolitan and intercity-scale distances. To this end, we derive closed-form analytical expressions for the expected fidelities and rates of end-to-end entanglement and teleported qubits as functions of relevant hardware parameters. Throughout, we adopt a simple noise model accounting for memory decoherence and a finite cut-off time. To determine the minimal requirements, we formulate the task as an optimisation problem over the parameters, where the analytical expressions enable efficient exploration of the parameter space without resorting to computationally intensive simulations. Using this approach, we obtain the minimal parameter values required to achieve the target teleportation fidelities of $2/3$ and 0.77. We perform the analysis in a hardware-agnostic manner, in which network performance is fully characterised by the elementary link generation probabilities, entanglement fidelities, and memory coherence time. We then evaluate it for a concrete case study based on trapped-ion parameters and model-based estimates for an ensemble-based backbone.

Within this framework, we address four questions: (i) the feasibility of reaching the classical benchmark for teleportation with fidelity $2/3$ over metropolitan-scale distances with present-day hardware; (ii) the metropolitan improvements required with backbone fixed at optimistic performance; (iii) the backbone improvements required with metropolitan network fixed at optimistic performance; and (iv) the minimal joint improvements necessary when both segments start from baseline performance over intercity-scale distances. We find that the classical benchmark is within reach of near-term advances in trapped-ion and ensemble-based platforms. In scenarios (ii) and (iii), ER teleportation already reaches the target fidelity of $2/3$ provided that at least one of the two segments operates in the optimistic regime. We also repeat the analysis for a higher target fidelity of 0.77, the midpoint between the classical limit and the highest teleportation fidelity attainable in the network under optimistic parameters in the ER case. The higher target fidelity is likewise reachable within all metropolitan and backbone parameter ranges, but it requires significant improvement in every scenario; in the QR case of (i) and in both ER and QR cases of (ii)–(iv), the coherence time and backbone fidelity are pushed close to their optimistic values.

Overall, the analysis shows that the most immediate experimental priority is to improve elementary link generation probabilities, while maintaining sufficiently high link fidelities and memory coherence times so that the increased generation rate does not come at the cost of excessive noise or decoherence. Achieving these values would require hardware improvements that are consistent with current near-term projections of experimental capabilities. Collectively, these findings establish clear design principles for making experimental progress: the elementary link generation probabilities in both metropolitan and backbone networks emerge as the most practical parameters to optimise, as the heuristic consistently favoured their improvement and drove them to optimistic values when necessary. This behaviour arises because the range of feasible improvements, from baseline to optimistic values, is smaller for the link generation probability parameters compared to others. However, it is important to emphasise that these optimistic estimates are obtained for individual parameters and do not always account for potential interdependencies among them. For instance, repeated photon generation attempts in trapped-ion systems can induce additional decoherence, thereby reducing the effective coherence time. Consequently, achieving all optimistic parameters simultaneously within a single device or experiment poses a significant challenge, and such analysis is left as future work. Building on this work, one can further investigate the performance of longer repeater chains, hardware requirements for more demanding applications such as blind quantum computation, and the conditions for simultaneously meeting target thresholds for teleportation rate and fidelity by appropriately modifying the cost function.

## Acknowledgments

S M, G A, and S W acknowledge funding from the Quantum Internet Alliance (QIA), which is supported by the European Union's Horizon Europe research and innovation programme under Grant Agreement No. 101102140 and project name 'QIA-Phase 1'. S W also acknowledges funding from NWO VICI. G A acknowledges funding from NSF CQN Grant No. 1941583, NSF Grant No. 2346089, and NSF Grant No. 2402861. We thank Anders S. Sørensen, Benedikt Tissot, Hugues de Riedmatten, Tracy

E. Northup, Benjamin P. Lanyon, and Victor Krutyanskiy for fruitful discussions. HdR, TN, BL, and VK provided parameter values in the state-of-the-art and optimistic regimes. We also thank Francisco Ferreira da Silva for critical feedback on the content of this manuscript and Michal van Hooft for advice and assistance with NetSquid.

## Data availability statement

The data that support the findings of this study are openly available at the following URL/DOI: https://doi.org/10.4121/6b7d42d3-ff78-4d64-bc9a-449480cc8550 [85].

Supplementary Notes available at: https://doi.org/10.1088/1367-2630/aeb40a/data1.

All source code used for data generation, processing, and plots is publicly available at [83].

## Author contribution

S M led the development and execution of the project. S M and S K performed the analytical work and prepared the manuscript. S M and G A worked on the simulations using NetSquid. S W conceived and supervised the project.

## Conflict of interest

The authors declare that they have no competing financial or personal interests that could have influenced the work reported in this paper.

## Appendix A. Derivation of teleportation rate and expected fidelity in the metropolitan network

In our model, teleportation in an MN proceeds by first generating entanglement between two end nodes in the same MN via HEG, followed by the teleportation step. We characterise the network by the entanglement generation probability, expected link fidelity, and coherence time of the end node memories. The teleportation rate is a function of the entanglement generation probability between end nodes at zero separation, i.e. the base efficiency, whose dependence on experimentally relevant quantities is given in appendix A.1. For the baseline and optimistic values, we use experimental and projected values, respectively, from trapped-ion platforms. Next, we derive the expressions for the teleportation rate and fidelity in appendix A.2 and A.3, respectively. Note that we do not model the entanglement fidelity as a function of experimental parameters but rather take its baseline value from the state-of-the-art experiment [53], and likewise treat the coherence time through the depolarising channel A2.

### A.1. Relating metropolitan entanglement generation probability to trapped-ion experiments

We now provide a detailed explanation of the hardware parameters of trapped-ion devices for remote entanglement generation [12, 53–55], while keeping the model deliberately simple so as to remain platform-agnostic under the assumptions **A1**–**A10**. The relevant parameters are

- **Photon collection efficiency from the ion** ($\eta_{\text{ion}}$): The probability that a photon emitted upon excitation is collected into the fibre, i.e. including every loss except detector and fibre transmission losses.
- **Detection efficiency of photons at ion frequency** ($\eta_{\text{det}}^{\text{ion-freq}}$): The efficiency of detectors optimised for the natural emission frequency of $Ca^+$ ions.
- **Frequency conversion efficiency, ion to telecom** ($\eta_{\text{FC}}$): The fraction of photons converted from the $Ca^+$ emission frequency to telecom frequency, including additional losses in fibre.
- **Detector efficiency at telecom frequency** ($\eta_{\text{det}}^{\text{telecom}}$): The probability of detecting a photon incident on the detector, without any other inefficiencies being included here.
- **Efficiency of using a 'truncated detection window'** ($\eta_{\text{penalty}}$): In the double-click protocol, a wider detection window allows for more photons but may include more noise, while a narrower window

**Table A1.** Baseline and optimistic parameter values from trapped-ion experiments. The optimistic values represent near-term technological advancements anticipated from current development trajectories and experimental progress rates, and are obtained in consultation with experimental physicists at the University of Innsbruck. The value of $\eta_{\text{penalty}} = 0.12$ is obtained from [53] by accepting 3.5 clicks per minute with a truncated detection window, instead of 0.49 clicks per second with an almost-whole detection window. We set both the baseline and optimistic value of $t_{\text{prep}}$ to be 175 $\mu$s, following the supplementary material of [12].

| Parameter | Baseline value | Optimistic value |
|---|---|---|
| $\eta_{\text{ion}}$ | 0.462/0.87 [84] | 0.5/0.87 [78] |
| $\eta_{\text{det}}^{\text{ion-freq}}$ | 0.87 [84] | 0.87 [78] |
| $\eta_{\text{FC}}$ | 0.25 [54] | 0.70 [78] |
| $\eta_{\text{penalty}}$ | 0.12 [53] | 0.20 [78] |
| $\eta_{\text{det}}^{\text{telecom}}$ | 0.75 [55] | 0.94 [78] |
| $t_{\text{prep}}$ | 175 $\mu$s [12] | 175 $\mu$s [12] |

improves fidelity but reduces the detection rate. The parameter $\eta_{\text{penalty}}$ quantifies the corresponding reduction in the ion–ion entanglement generation probability due to this truncation.

- **Average preparation time between shots** ($t_{\text{prep}}$): The average local overhead associated with sequential photon generation via laser excitation, including cycle delays due to initialisation, cooling, optical pumping, and related operations.

Recall from (5) that, with the two end nodes separated by a distance $2d'_{\text{m}}$ and the hub at the midpoint (see figure 1), the average time per entanglement generation attempt is $t_{\text{m}'} = t_{\text{prep}} + 2t_{\text{m}}^{\text{class}}$, where $t_{\text{m}}^{\text{class}} = d_{\text{m}'}/v$ and $v$ is the speed of light in fibre. Under the assumption A4, we adopt the double-click HEG protocol [67]. In this protocol, both end nodes, here trapped ions, generate matter–photon entanglement and emit photons that are collected with efficiency $\eta_{\text{ion}}$ and frequency-converted with efficiency $\eta_{\text{FC}}$. The photons are then sent towards the hub where they interfere and are detected with efficiency $\eta_{\text{det}}^{\text{telecom}}$; a two-photon detection event heralds node-to-node entanglement. Thus, with a truncated detection window, the base efficiency is

$$p_{\text{m}}^0 = \frac{1}{2}\,\eta_{\text{penalty}}\left(\eta_{\text{ion}}\,\eta_{\text{FC}}\,\eta_{\text{det}}^{\text{telecom}}\right)^2 . \tag{A.1}$$

Substituting the parameter values from table A1 into (A.1) yields the baseline and optimistic base efficiencies of $5.95 \times 10^{-4}$ and $1.43 \times 10^{-2}$, respectively. The generation probability at separation $2d_{\text{m}'}$ (km) then follows from (4) as

$$p_{\text{m}'} = p_{\text{m}}^0 10^{-2\alpha d_{\text{m}'}/10} .$$

Note that we neglect additional factors such as imperfect indistinguishability, non-photon-number-resolving detectors, and detector dark counts [24], absorbing such effects into the link fidelity instead.

### A.2. Teleportation rate in the metropolitan network

In our model, the rate at which a qubit can be teleported between end nodes in an MN is determined by the time to establish a link and the subsequent teleportation time. Since data qubit preparation is instantaneous (see **A10**), the teleportation time includes the transmission time $2t_{\text{m}}^{\text{class}}$ of the Pauli correction message from sender to receiver (see **A4**). Further, let the random variable $X_{\text{m}'}$ represent the time to establish a node-to-node entanglement successfully. Hence, the total time required in both ER and QR cases is $2t_{\text{m}}^{\text{class}} + X_{\text{m}'}$, and the rate is

$$R_{\text{m}} = \frac{1}{\mathbb{E}\left(2t_{\text{m}}^{\text{class}} + X_{\text{m}'}\right)} = \frac{1}{2t_{\text{m}}^{\text{class}} + \mathbb{E}\left(X_{\text{m}'}\right)} . \tag{A.2}$$

Let $M'$ be the number of attempts to create a link in the MN, and $M' \sim \text{Geo}(p_{\text{m}'})$ (see (6)), such that $X_{\text{m}'} = t_{\text{m}'}M'$. Hence, we have

$$R_{\text{m}} = \frac{1}{2t_{\text{m}}^{\text{class}} + \mathbb{E}\left(t_{\text{m}'}M'\right)} \overset{\text{(i)}}{=} \frac{1}{2t_{\text{m}}^{\text{class}} + t_{\text{m}'}/p_{\text{m}'}} = \frac{p_{\text{m}'}}{2p_{\text{m}'}t_{\text{m}}^{\text{class}} + t_{\text{m}'}} , \tag{A.3}$$

where in (i), we used $\mathbb{E}(M') = 1/p_{\mathrm{m}'}$, for geometric distribution. Since the HEG process and hardware parameters are related to trapped-ion experiments [12, 53–55], the derivation of the entanglement generation probability $p_{\mathrm{m}'}$ is given in appendix A.1, and the state-of-the-art and optimistic values are presented in table A1.

### A.3. Expected teleportation fidelity in the metropolitan network

In ER teleportation, we teleport a pure state once a link of fidelity $f_{\mathrm{m}'}$, or corresponding Werner parameter $w_{\mathrm{m}'} = (4f_{\mathrm{m}'} - 1)/3$, is ready. Observe that in the ER case, the link fidelity is deterministic. Thus, using (B.4), the expected teleportation fidelity is given by

$$F_{\mathrm{m}}^{\mathrm{ER}} = \frac{1 + w_{\mathrm{m}'} \mathrm{e}^{-2t_{\mathrm{m}}^{\mathrm{class}}/t_{\mathrm{coh}}}}{2} . \tag{A.4}$$

In the QR case, the data qubit is initially prepared at the sender node and stored in memory, where it decoheres until a link is ready. This waiting time for one teleportation round is given by $X_{\mathrm{m}'} = t_{\mathrm{m}'} M'$, where $M'$ is the number of link generation attempts until success. Thus, from (B.4), we obtain the expected fidelity in QR teleportation as

$$F_{\mathrm{m}}^{\mathrm{QR}} = \mathbb{E}\left(\frac{1 + w_{\mathrm{m}'} \mathrm{e}^{-X_{\mathrm{m}'}/t_{\mathrm{coh}}} \mathrm{e}^{-2t_{\mathrm{m}}^{\mathrm{class}}/t_{\mathrm{coh}}}}{2}\right) \tag{A.5}$$

$$= \frac{1}{2} + \frac{1}{2} w_{\mathrm{m}'} \mathrm{e}^{-2t_{\mathrm{m}}^{\mathrm{class}}/t_{\mathrm{coh}}} \mathbb{E}\left(\mathrm{e}^{-t_{\mathrm{m}'} M'/t_{\mathrm{coh}}}\right) \tag{A.6}$$

$$= \frac{1}{2} + \frac{1}{2} w_{\mathrm{m}'} \mathrm{e}^{-2t_{\mathrm{m}}^{\mathrm{class}}/t_{\mathrm{coh}}} \frac{p_{\mathrm{m}'}}{\mathrm{e}^{t_{\mathrm{m}'}/t_{\mathrm{coh}}} + p_{\mathrm{m}'} - 1} . \tag{A.7}$$

## Appendix B. Teleporting a mixed state using a Werner state

**Lemma 2.** *Consider the teleportation of a data qubit in a mixed state*

$$\rho_{\mathrm{data}} = p_d |\phi\rangle\langle\phi| + (1 - p_d) \frac{\mathbb{I}_2}{2}, \tag{B.1}$$

*where $p_d \in [0, 1]$ is the probability weight of the pure state $|\phi\rangle$ and $\mathbb{I}_2$ is the $2 \times 2$ identity matrix. Suppose Alice and Bob share an entangled resource described by the Werner state*

$$\rho_w = w \left|\Phi^+\right\rangle\left\langle\Phi^+\right| + (1 - w) \frac{\mathbb{I}_4}{4}, \tag{B.2}$$

*where $|\Phi^+\rangle$ is the maximally entangled Bell state, $w \in [0, 1]$ is the corresponding Werner parameter and $\mathbb{I}_4$ is the $4 \times 4$ identity matrix. Assume that each qubit is subject to decoherence modelled by a depolarising channel $\mathcal{E}_t$ acting as*

$$\mathcal{E}_t(|\psi\rangle\langle\psi|) = \mathrm{e}^{-t/t_{\mathrm{coh}}} |\psi\rangle\langle\psi| + \left(1 - \mathrm{e}^{-t/t_{\mathrm{coh}}}\right) \frac{\mathbb{I}_2}{2}, \tag{B.3}$$

*with coherence time $t_{\mathrm{coh}}$ and storage duration $t$. Further, assume that local operations are instantaneous compared to classical communication and entanglement generation times, so that the time for Bell measurement and application of Pauli corrections is negligible. Then, the fidelity of the teleported qubit with respect to $|\phi\rangle$ is given by*

$$F_{\mathrm{tel}} = \frac{1 + w p_d \mathrm{e}^{-t_{\mathrm{class}}/t_{\mathrm{coh}}}}{2} , \tag{B.4}$$

*where $t_{\mathrm{class}}$ denotes the classical communication time required to transmit the Pauli correction message.*

**Proof.** See Supplementary Note D [82]. □

## Appendix C. Proof of theorem 1

In this appendix, we prove theorem 1, which gives the expected time to successfully establish an end-to-end link. The corresponding rate of teleportation in the IN then follows from (23).

**Proof.** With $N$ denoting the number of rounds required for end-to-end link generation, we have

$$\mathbb{E}(X_{\mathrm{e2e}}) = \mathbb{E}\left(\sum_{i=1}^{N} Z^{(i)}\right) \tag{C.1}$$

$$\overset{\text{(i)}}{=} \mathbb{E}\left(\mathbb{E}\left(\sum_{i=1}^{N} Z^{(i)} \mid N\right)\right) \tag{C.2}$$

$$\overset{\text{(ii)}}{=} \sum_{n=1}^{\infty} p(1-p)^{n-1}\,\mathbb{E}\left(\sum_{i=1}^{N} Z^{(i)} \mid N=n\right) \tag{C.3}$$

$$\overset{\text{(iii)}}{=} \sum_{n=1}^{\infty} p(1-p)^{n-1}\left(\sum_{i=1}^{n-1}\mathbb{E}\left(Z^{(i)} \mid Y^{(i)}=0\right) + \mathbb{E}\left(Z^{(n)} \mid Y^{(n)}=1\right)\right) \tag{C.4}$$

$$\overset{\text{(iv)}}{=} \sum_{n=1}^{\infty} p(1-p)^{n-1}\left((n-1)\,\mathbb{E}(Z \mid Y=0) + \mathbb{E}(Z \mid Y=1)\right) \tag{C.5}$$

$$\overset{\text{(v)}}{=} \left(\frac{1}{p}-1\right)\frac{\mathbb{E}(Z\mathbb{1}_{Y=0})}{\mathbb{P}(Y=0)} + \frac{\mathbb{E}(Z\mathbb{1}_{Y=1})}{\mathbb{P}(Y=1)} \tag{C.6}$$

$$= \frac{\mathbb{E}(Z\mathbb{1}_{Y=0}) + \mathbb{E}(Z\mathbb{1}_{Y=1})}{p}\,, \tag{C.7}$$

which establishes (31). Here, (i) and (v) use the definition of conditional expectation, (ii) uses $N \sim \mathrm{Geo}(p)$, (iii) uses linearity of expectation and (iv) follows from the fact that $Y^{(i)} \overset{\text{iid}}{\sim} Y$ and $Z^{(i)} \overset{\text{iid}}{\sim} Z$.

To show (32) and (33), we use the principle of inclusion and exclusion. Recalling the definitions of $A_i^+$'s and $A_i^+A_j^+$'s from (29),

$$\begin{aligned}\mathbb{E}(Z\mathbb{1}_{Y=1}) &= \mathbb{E}\left(Z\mathbb{1}_{A_1^+}\right) + \mathbb{E}\left(Z\mathbb{1}_{A_2^+}\right) + \mathbb{E}\left(Z\mathbb{1}_{A_{\mathrm{b}}^+}\right) - \mathbb{E}\left(Z\mathbb{1}_{A_1^+A_2^+}\right) - \mathbb{E}\left(Z\mathbb{1}_{A_1^+A_{\mathrm{b}}^+}\right)\\ &\quad - \mathbb{E}\left(Z\mathbb{1}_{A_2^+A_{\mathrm{b}}^+}\right) + \mathbb{E}\left(Z\mathbb{1}_{A_1^+A_2^+A_{\mathrm{b}}^+}\right)\\ &\overset{\text{(i)}}{=} 2\mathbb{E}\left(Z\mathbb{1}_{A_1^+}\right) + \mathbb{E}\left(Z\mathbb{1}_{A_{\mathrm{b}}^+}\right) - \mathbb{E}\left(Z\mathbb{1}_{A_1^+A_2^+}\right) - 2\mathbb{E}\left(Z\mathbb{1}_{A_1^+A_{\mathrm{b}}^+}\right)\\ &\quad + \mathbb{E}\left(Z\mathbb{1}_{A_1^+A_2^+A_{\mathrm{b}}^+}\right)j,\end{aligned} \tag{C.8}$$

where (i) follows from the symmetry of the metropolitan links. For $Y=0$, we similarly have

$$\begin{aligned}\mathbb{E}(Z\mathbb{1}_{Y=0}) &= 2\mathbb{E}\left(Z\mathbb{1}_{A_1^-}\right) + \mathbb{E}\left(Z\mathbb{1}_{A_{\mathrm{b}}^-}\right) - \mathbb{E}\left(Z\mathbb{1}_{A_1^-A_2^-}\right) - 2\mathbb{E}\left(Z\mathbb{1}_{A_1^-A_{\mathrm{b}}^-}\right)\\ &\quad + \mathbb{E}\left(Z\mathbb{1}_{A_1^-A_2^-A_{\mathrm{b}}^-}\right)\\ &\overset{\text{(i)}}{=} 2\left(\mathbb{E}\left(Z\mathbb{1}_{A_{12}^-}\right) + \mathbb{E}\left(Z\mathbb{1}_{A_{1\mathrm{b}}^-}\right) - \mathbb{E}\left(Z\mathbb{1}_{A_{12}^-A_{1\mathrm{b}}^-}\right)\right) + 2\mathbb{E}\left(Z\mathbb{1}_{A_{\mathrm{b}1}^-}\right)\\ &\quad - \mathbb{E}\left(Z\mathbb{1}_{A_{\mathrm{b}1}^-A_{\mathrm{b}2}^-}\right) - \mathbb{E}\left(Z\mathbb{1}_{A_1^-A_2^-}\right) - 2\mathbb{E}\left(Z\mathbb{1}_{A_1^-A_{\mathrm{b}}^-}\right)\,.\end{aligned} \tag{C.9}$$

Note that $\mathbb{E}\left(Z\mathbb{1}_{A_1^-A_2^-A_{\mathrm{b}}^-}\right) = 0$, as the subset $A_1^-A_2^-A_{\mathrm{b}}^-$ is empty and (i) uses inclusion and exclusion as the events $A_i^-$ are determined via $X_{\max}$, while $Z|Y=0 \sim X_{\min} + t_{\mathrm{cut}}$. Specifically, we have

$$\mathbb{1}_{A_1^-} = \mathbb{1}_{A_{12}^-} + \mathbb{1}_{A_{1\mathrm{b}}^-} - \mathbb{1}_{A_{12}^-A_{1\mathrm{b}}^-}\,, \quad \mathbb{1}_{A_{\mathrm{b}}^-} = \mathbb{1}_{A_{\mathrm{b}1}^-} + \mathbb{1}_{A_{\mathrm{b}2}^-} - \mathbb{1}_{A_{\mathrm{b}1}^-A_{\mathrm{b}2}^-}\,. \tag{C.10}$$

Also by symmetry, $\mathbb{E}\left(Z\mathbb{1}_{A_{\mathrm{b}1}^-}\right) = \mathbb{E}\left(Z\mathbb{1}_{A_{\mathrm{b}2}^-}\right)$. We have thus established (32) and (33). □

**Table D1.** Derivation of the Werner parameter of the end-to-end entangled state. In the last column, we include the constant communication delay $t_{\mathrm{msg}}$, which accounts for the time required to transmit the final swap message from border nodes to both end nodes. We set $k = 2/t_{\mathrm{coh}}$. Note that due to symmetry of the metropolitan links, the contributions from the events $A_{21}^{+}$, $A_{2b}^{+}$, and $A_{\mathrm{b2}}^{+}$ are identical to those from $A_{12}^{+}$, $A_{1\mathrm{b}}^{+}$, and $A_{\mathrm{b1}}^{+}$, respectively. The final column is precisely $w_{\mathrm{m}}^{2} w_{\mathrm{b}} \mathrm{e}^{-k(X_{\mathrm{diff}}+t_{\mathrm{msg}})}$; see (36).

| Set | $X_{\mathrm{min}}$ | $X_{\mathrm{mid}}$ | $X_{\mathrm{max}}$ | End-to-end link |
|---|---|---|---|---|
| $A_{12}^{+}$ | link 2: $w_{\mathrm{m}}$ | link 2: $w_{\mathrm{m}}\mathrm{e}^{-k(X_{\mathrm{b}}-X_2)}$<br>link b: $w_{\mathrm{b}}$<br>link b2: $w_{\mathrm{m}}w_{\mathrm{b}}\mathrm{e}^{-k(X_{\mathrm{b}}-X_2)}$ | link b2: $w_{\mathrm{m}}w_{\mathrm{b}}\mathrm{e}^{-k(X_1-X_2)}$<br>link 1: $w_{\mathrm{m}}$<br>link 1b2: $w_{\mathrm{m}}^{2}w_{\mathrm{b}}\mathrm{e}^{-k(X_1-X_2)}$ | $w_{\mathrm{m}}^{2}w_{\mathrm{b}}\mathrm{e}^{-k(X_1-X_2)}$<br>$\cdot\,\mathrm{e}^{-kt_{\mathrm{msg}}}$ |
| $A_{1\mathrm{b}}^{+}$ | link b: $w_{\mathrm{b}}$ | link b: $w_{\mathrm{b}}\mathrm{e}^{-k(X_2-X_{\mathrm{b}})}$<br>link 2: $w_{\mathrm{m}}$<br>link b2: $w_{\mathrm{m}}w_{\mathrm{b}}\mathrm{e}^{-k(X_2-X_{\mathrm{b}})}$ | link b2: $w_{\mathrm{m}}w_{\mathrm{b}}\mathrm{e}^{-k(X_1-X_{\mathrm{b}})}$<br>link 1: $w_{\mathrm{m}}$<br>link 1b2: $w_{\mathrm{m}}^{2}w_{\mathrm{b}}\mathrm{e}^{-k(X_1-X_{\mathrm{b}})}$ | $w_{\mathrm{m}}^{2}w_{\mathrm{b}}\mathrm{e}^{-k(X_1-X_{\mathrm{b}})}$<br>$\cdot\,\mathrm{e}^{-kt_{\mathrm{msg}}}$ |
| $A_{\mathrm{b1}}^{+}$ | link 1: $w_{\mathrm{m}}$ | link 1: $w_{\mathrm{m}}\mathrm{e}^{-k(X_2-X_1)}$<br>link 2: $w_{\mathrm{m}}$<br><br>swap not possible | link 1: $w_{\mathrm{m}}\mathrm{e}^{-k(X_{\mathrm{b}}-X_1)}$<br>link 2: $w_{\mathrm{m}}\mathrm{e}^{-k(X_{\mathrm{b}}-X_2)}$<br>link b: $w_{\mathrm{b}}$<br>link 1b2:<br>$w_{\mathrm{m}}^{2}w_{\mathrm{b}}\mathrm{e}^{-k(2X_{\mathrm{b}}-X_1-X_2)}$ | $w_{\mathrm{m}}^{2}w_{\mathrm{b}}\mathrm{e}^{-k(2X_{\mathrm{b}}-X_1-X_2)}$<br>$\cdot\,\mathrm{e}^{-kt_{\mathrm{msg}}}$ |

## Appendix D. Proof of Lemma 1

Here, we prove lemma 1, which gives the expected fidelity of an end-to-end link in the IN.

**Proof.** Recall from R1 that $X_1$, $X_2$, and $X_{\mathrm{b}}$ are the durations of successfully generating entanglement between $\mathrm{P}_1$ (or $\mathrm{P}_2$) and $\mathrm{B}_1$, $\mathrm{P}_3$ (or $\mathrm{P}_4$) and $\mathrm{B}_2$, and $\mathrm{B}_1$ and $\mathrm{B}_2$, respectively. Furthermore, recall from **A1** that an entanglement swap between two Werner states results in a Werner state with the corresponding Werner parameter being the product of those of the initial states. Since decoherence affects the states and the effect depends on the chronological order of the generation times, the end-to-end link fidelity differs across the events defined in (29) and (30). We describe the evolution of the Werner parameter for each case in table D1.

Since unsuccessful trials do not influence the fidelity of the final end-to-end entangled link, we restrict our analysis to the case $Y = 1$. In this case, we use the shorthand $X_{\mathrm{diff}}$ introduced in (36) to succinctly express the contribution of different sub-events by

$$w_{\mathrm{e2e}} = w_{\mathrm{m}}^{2} w_{\mathrm{b}} \mathrm{e}^{-k\left(X_{\mathrm{diff}}+t_{\mathrm{msg}}\right)}\,, \tag{D.1}$$

see table D1 for an explanation. Thus, we obtain the expected Werner parameter of the end-to-end link as

$$\begin{aligned}
\mathbb{E}\left(w_{\mathrm{e2e}}\right) &= \mathbb{E}\left(w_{\mathrm{m}}^{2} w_{\mathrm{b}} \mathrm{e}^{-k\left(X_{\mathrm{diff}}+t_{\mathrm{msg}}\right)} \mid Y=1\right) && \text{(D.2)}\\
&= w_{\mathrm{m}}^{2} w_{\mathrm{b}} \mathrm{e}^{-kt_{\mathrm{msg}}} \frac{\mathbb{E}\left(\mathrm{e}^{-kX_{\mathrm{diff}}} \mathbb{1}_{Y=1}\right)}{\mathbb{P}\left(Y=1\right)} \\
&\overset{(26),(35)}{=} \frac{w_{\mathrm{m}}^{2} w_{\mathrm{b}} \mathrm{e}^{-kt_{\mathrm{msg}}}}{p} U_1\left(k\right)\,, && \text{(D.3)}
\end{aligned}$$

and the corresponding expected fidelity is $(1+3\mathbb{E}(w_{\mathrm{e2e}}))/4$, which establishes (34).

To show (37), we use the principle of inclusion and exclusion. Recalling the definitions of $A_i^{+}$ and $A_{ij}^{+}$ from (29), we have

$$\begin{aligned}
U_1\left(\nu\right) &= \mathbb{E}\left(\mathrm{e}^{-\nu X_{\mathrm{diff}}} \mathbb{1}_{Y=1}\right) && \text{(D.4)}\\
&= \mathbb{E}\left(\mathrm{e}^{-\nu X_{\mathrm{diff}}} \mathbb{1}_{A_1^{+}}\right) + \mathbb{E}\left(\mathrm{e}^{-\nu X_{\mathrm{diff}}} \mathbb{1}_{A_2^{+}}\right) + \mathbb{E}\left(\mathrm{e}^{-\nu X_{\mathrm{diff}}} \mathbb{1}_{A_{\mathrm{b}}^{+}}\right) - \mathbb{E}\left(\mathrm{e}^{-\nu X_{\mathrm{diff}}} \mathbb{1}_{A_1^{+}A_2^{+}}\right) \\
&\quad - \mathbb{E}\left(\mathrm{e}^{-\nu X_{\mathrm{diff}}} \mathbb{1}_{A_1^{+}A_{\mathrm{b}}^{+}}\right) - \mathbb{E}\left(\mathrm{e}^{-\nu X_{\mathrm{diff}}} \mathbb{1}_{A_2^{+}A_{\mathrm{b}}^{+}}\right) + \mathbb{E}\left(\mathrm{e}^{-\nu X_{\mathrm{diff}}} \mathbb{1}_{A_1^{+}A_2^{+}A_{\mathrm{b}}^{+}}\right) \\
&\overset{(\mathrm{i})}{=} 2\left(\mathbb{E}\left(\mathrm{e}^{-\nu\left(X_1-X_2\right)} \mathbb{1}_{A_{12}^{+}}\right) + \mathbb{E}\left(\mathrm{e}^{-\nu\left(X_1-X_{\mathrm{b}}\right)} \mathbb{1}_{A_{1\mathrm{b}}^{+}}\right) - \mathbb{E}\left(\mathrm{e}^{-\nu\left(X_1-X_2\right)} \mathbb{1}_{A_{12}^{+}A_{1\mathrm{b}}^{+}}\right)\right) \\
&\quad + \mathbb{E}\left(\mathrm{e}^{-\nu\left(2X_{\mathrm{b}}-X_1-X_2\right)} \mathbb{1}_{A_{\mathrm{b}}^{+}}\right) \\
&\quad - \mathbb{E}\left(\mathrm{e}^{-\nu\left(X_1-X_{\mathrm{b}}\right)} \mathbb{1}_{A_1^{+}A_2^{+}}\right) - 2\mathbb{E}\left(\mathrm{e}^{-\nu\left(X_1-X_2\right)} \mathbb{1}_{A_1^{+}A_{\mathrm{b}}^{+}}\right) + \mathbb{E}\left(\mathbb{1}_{A_1^{+}A_2^{+}A_{\mathrm{b}}^{+}}\right)\,, && \text{(D.5)}
\end{aligned}$$

where (i) follows from the symmetry of the metropolitan links and we used the principle of inclusion and exclusion for the event $A_1^+$ since $A_1^+$ is defined via $X_{\max}$, while $X_{\text{diff}} = X_{\max} - X_{\min}$ for $A_1^+$ (see (36)). Specifically, we have

$$\mathbb{1}_{A_1^+} = \mathbb{1}_{A_{12}^+} + \mathbb{1}_{A_{1\text{b}}^+} - \mathbb{1}_{A_{12}^+ A_{1\text{b}}^+}\,, \tag{D.6}$$

Furthermore, we have substituted the value of $X_{\text{diff}}$ from (36). Note that, for $A_1^+ A_2^+ A_{\text{b}}^+$, we have $X_{\text{diff}} = 0$ which follows from the definition (36). Thus, we have established (37). □

## Appendix E. Proof of Theorem 3

Here, we prove theorem 3, which gives the expected teleportation fidelity in the QR case.

**Proof.** In the QR case, the data qubit is first prepared at the sender node in a pure state, and the end-to-end link generation process begins immediately. If $N$ denotes the total number of required rounds until success, the data qubit experiences decoherence over the $N-1$ failed rounds, of durations $Z_0^{(i)} \overset{\text{iid}}{\sim} Z \mid Y=0$, and over the successful round, of duration $Z_1 \sim Z \mid Y=1$; see (27). Therefore, at the beginning of teleportation, the data qubit is in the state

$$p_d \left|\phi\right\rangle\left\langle\phi\right| + (1-p_d)\frac{\mathbb{I}_2}{2}\,, \text{ where } p_d := \mathrm{e}^{-\left(\sum_{i=1}^{N-1} Z_0^{(i)} + Z_1\right)/t_{\text{coh}}} = \mathrm{e}^{-k\left(\sum_{i=1}^{N-1} Z_0^{(i)} + Z_1\right)/2},\ k = 2/t_{\text{coh}}. \tag{E.1}$$

After the BSM on the data qubit and one-half of the end-to-end link, the qubit stored in the receiver node memory decoheres during the propagation time $t_{\text{int}}^{\text{class}}$ of the Pauli correction message. Therefore, using (B.4), we obtain the expected fidelity of the teleported qubit as

$$\begin{aligned}
&\mathbb{E}\left(\frac{1 + w_{\text{e2e}}\mathrm{e}^{-k\left(\sum_{i=1}^{N-1} Z_0^{(i)} + Z_1\right)/2}\mathrm{e}^{-kt_{\text{int}}^{\text{class}}/2}}{2}\right) \\
&\overset{(34)}{=} \frac{1}{2} + \frac{1}{2}w_{\text{m}}^2 w_{\text{b}}\mathrm{e}^{-k\left(t_{\text{msg}} + t_{\text{int}}^{\text{class}}/2\right)} \underbrace{\mathbb{E}\left(\mathrm{e}^{-k\sum_{i=1}^{N-1} Z_0^{(i)}/2}\right)\mathbb{E}\left(\mathrm{e}^{-k(X_{\text{diff}} + Z_1/2)}\right)}_{=:\,U'}\,.
\end{aligned} \tag{E.2}$$

Recall from (26) that $p = \mathbb{P}(Y=1)$. Now the term $U'$ in (E.2) can be simplified as

$$\begin{aligned}
U' &= \sum_{n=1}^{\infty} p(1-p)^{n-1}\left(\mathbb{E}\left(\mathrm{e}^{-kZ_0/2}\right)\right)^{n-1}\mathbb{E}\left(\mathrm{e}^{-k(X_{\text{diff}} + Z_1/2)}\right) && \text{(E.3)}\\
&= \frac{p\mathbb{E}\left(\mathrm{e}^{-k(X_{\text{diff}} + Z_1/2)}\right)}{1-(1-p)\mathbb{E}\left(\mathrm{e}^{-kZ_0/2}\right)} && \text{(E.4)}\\
&= \frac{\mathbb{E}\left(\mathrm{e}^{-k(X_{\text{diff}} + Z/2)}\mathbb{1}_{Y=1}\right)}{1-\mathbb{E}\left(\mathrm{e}^{-kZ/2}\mathbb{1}_{Y=0}\right)} && \text{(E.5)}\\
&\overset{(27)}{=} \frac{\mathrm{e}^{-kt_{\text{msg}}/2}\mathbb{E}\left(\mathrm{e}^{-k(X_{\text{diff}} + X_{\max}/2)}\mathbb{1}_{Y=1}\right)}{1-\mathrm{e}^{-kt_{\text{cut}}/2}\mathbb{E}\left(\mathrm{e}^{-kX_{\min}/2}\mathbb{1}_{Y=0}\right)} && \text{(E.6)}\\
&\overset{(41),(42)}{=} \frac{\mathrm{e}^{-kt_{\text{msg}}/2}U_2(k)}{1-\mathrm{e}^{-kt_{\text{cut}}/2}U_3(k)}\,. && \text{(E.7)}
\end{aligned}$$

Substituting (E.7) in (E.2) establishes (40). To show (43) and (44), we use the principle of inclusion and exclusion. Recalling the definitions of $A_i^+$ and $A_{ij}^+$ from (29), we have

$$\begin{aligned}
U_2(v) &= \mathbb{E}\left(\mathrm{e}^{-v(X_{\text{diff}} + X_{\max}/2)}\mathbb{1}_{Y=1}\right)\\
&\overset{(i)}{=} 2\left(\mathbb{E}\left(\mathrm{e}^{-v(3X_1/2 - X_2)}\mathbb{1}_{A_{12}^+}\right) + \mathbb{E}\left(\mathrm{e}^{-v(3X_1/2 - X_{\text{b}})}\mathbb{1}_{A_{1\text{b}}^+}\right) - \mathbb{E}\left(\mathrm{e}^{-v(3X_1/2 - X_2)}\mathbb{1}_{A_{12}^+ A_{1\text{b}}^+}\right)\right)\\
&\quad + \mathbb{E}\left(\mathrm{e}^{-v(5X_{\text{b}}/2 - X_1 - X_2)}\mathbb{1}_{A_{\text{b}}^+}\right) - \mathbb{E}\left(\mathrm{e}^{-v(3X_1/2 - X_{\text{b}})}\mathbb{1}_{A_1^+ A_2^+}\right) - 2\mathbb{E}\left(\mathrm{e}^{-v(3X_1/2 - X_2)}\mathbb{1}_{A_1^+ A_{\text{b}}^+}\right)\\
&\quad + \mathbb{E}\left(\mathrm{e}^{-vX_1/2}\mathbb{1}_{A_1^+ A_2^+ A_{\text{b}}^+}\right)\,,
\end{aligned} \tag{E.8}$$

where (i) follows from the symmetry of the metropolitan links, uses inclusion and exclusion on $A_1^+$ via (D.6), and expands the shorthand $X_{\text{diff}}$ from (36). This establishes (43). Similarly, we can expand $U_3(v)$ as

$$\begin{aligned} U_3(v) &= \mathbb{E}\left(\mathrm{e}^{-vX_{\min}/2}\mathbb{1}_{Y=0}\right) \\ &\overset{\text{(i)}}{=} 2\left(\mathbb{E}\left(\mathrm{e}^{-vX_2/2}\mathbb{1}_{A_{12}^-}\right)+\mathbb{E}\left(\mathrm{e}^{-vX_{\mathrm{b}}/2}\mathbb{1}_{A_{1\mathrm{b}}^-}\right)-\mathbb{E}\left(\mathrm{e}^{-vX_2/2}\mathbb{1}_{A_{12}^-A_{1\mathrm{b}}^-}\right)\right) \\ &\quad+2\mathbb{E}\left(\mathrm{e}^{-vX_1/2}\mathbb{1}_{A_{\mathrm{b}1}^-}\right)-\mathbb{E}\left(\mathrm{e}^{-vX_1/2}\mathbb{1}_{A_{\mathrm{b}1}^-A_{\mathrm{b}2}^-}\right)-\mathbb{E}\left(\mathrm{e}^{-vX_{\mathrm{b}}/2}\mathbb{1}_{A_1^-A_2^-}\right) \\ &\quad-2\mathbb{E}\left(\mathrm{e}^{-vX_2/2}\mathbb{1}_{A_1^-A_{\mathrm{b}}^-}\right), \end{aligned} \tag{E.9}$$

where the term $\mathbb{1}_{A_1^-A_2^-A_{\mathrm{b}}^-}$ is omitted since $A_1^-A_2^-A_{\mathrm{b}}^-$ is empty, and (i) uses the symmetry of the metropolitan links, under which $\mathbb{E}\left(\mathrm{e}^{-vX_1/2}\mathbb{1}_{A_{\mathrm{b}1}^-}\right)=\mathbb{E}\left(\mathrm{e}^{-vX_2/2}\mathbb{1}_{A_{\mathrm{b}2}^-}\right)$, together with inclusion and exclusion via (C.10) since the events $A_i^-$ are determined by $X_{\max}$ while here we need $X_{\min}$. Thus, we have established (44) by plugging in the value of $X_{\min}$. □

## ORCID iDs

Soubhadra Maiti 0000-0002-3824-4495
Guus Avis 0000-0001-7035-8065
Sounak Kar 0000-0002-0989-8596
Stephanie Wehner 0000-0002-8433-0730

## References

[1] Wehner S, Elkouss D and Hanson R 2018 Quantum internet: a vision for the road ahead *Science* **362** eaam9288
[2] Ekert A K 1991 Quantum cryptography based on bell's theorem *Phys. Rev. Lett.* **67** 661–3
[3] Bennett C H, Brassard G and Mermin N D 1992 Quantum cryptography without Bell's theorem *Phys. Rev. Lett.* **68** 557
[4] Giovannetti V, Lloyd S and Maccone L 2004 Quantum-enhanced measurements: beating the standard quantum limit *Science* **306** 1330–6
[5] Broadbent A, Fitzsimons J and Kashefi E 2009 Universal blind quantum computation *2009 50th Annual IEEE Symp. on Foundations of Computer Science* (IEEE) pp 517–26
[6] Jozsa R, Abrams D S, Dowling J P and Williams C P 2000 Quantum clock synchronization based on shared prior entanglement *Phys. Rev. Lett.* **85** 2010
[7] Bell J S 1964 On the Einstein Podolsky Rosen paradox *Phys. Phys. Fiz.* **1** 195
[8] Borregaard J and Pikovski I 2025 Testing quantum theory on curved spacetime with quantum networks *Phys. Rev. Res.* **7** 023192
[9] Wootters W K and Zurek W H 1982 A single quantum cannot be cloned *Nature* **299** 802–3
[10] Briegel H-J, Dür W, Cirac J I and Zoller P 1998 Quantum repeaters: the role of imperfect local operations in quantum communication *Phys. Rev. Lett.* **81** 5932
[11] Moehring D L, Maunz P, Olmschenk S, Younge K C, Matsukevich D N, Duan L-M and Monroe C 2007 Entanglement of single-atom quantum bits at a distance *Nature* **449** 68–71
[12] Krutyanskiy V, Canteri M, Meraner M, Bate J, Krcmarsky V, Schupp J, Sangouard N and Lanyon B P 2023 Telecom-wavelength quantum repeater node based on a trapped-ion processor *Phys. Rev. Lett.* **130** 213601
[13] Bernien H *et al* 2013 Heralded entanglement between solid-state qubits separated by three metres *Nature* **497** 86–90
[14] Lago-Rivera D, Grandi S, Rakonjac J V, Seri A and de Riedmatten H 2021 Telecom-heralded entanglement between multimode solid-state quantum memories *Nature* **594** 37–40
[15] Chou C-W, Laurat J, Deng H, Choi K S, De Riedmatten H, Felinto D and Kimble H J 2007 Functional quantum nodes for entanglement distribution over scalable quantum networks *Science* **316** 1316–20
[16] Tissot B, Maiti S, Hellebek E R and Sørensen A S 2026 Hybrid single-ion atomic-ensemble node for high-rate remote entanglement generation *Phys. Rev. A* **114** L010602
[17] Tissot B, Maiti S, Hellebek E and Sørensen A S 2026 Single- and double-click high-rate entanglement generation between distant ions using multiplexed atomic ensembles *Phys. Rev. Res.* **8** 033067
[18] Sun S, Bhatti D, Gao S, Elkouss D and Takahashi H 2025 Hybrid quantum repeater chains with atom-based quantum processing units and quantum memory multiplexers (arXiv:2512.21655)
[19] Pompili M *et al* 2021 Realization of a multinode quantum network of remote solid-state qubits *Science* **372** 259–64
[20] Goodenough K, Coopmans T and Towsley D 2025 On noise in swap asap repeater chains: exact analytics, distributions and tight approximations *Quantum* **9** 1744
[21] de Andrade M G, Van Milligen E A, Bacciottini L, Chandra A, Pouryousef S, Panigrahy N K, Vardoyan G and Towsley D 2024 On the analysis of quantum repeater chains with sequential swaps (arXiv:2405.18252)
[22] Rozpedek F, Goodenough K, Ribeiro J, Kalb N, Vivoli V C, Reiserer A, Hanson R, Wehner S and Elkouss D 2018 Parameter regimes for a single sequential quantum repeater *Quantum Sci. Technol.* **3** 034002
[23] da Silva F F, Torres-Knoop A, Coopmans T, Maier D and Wehner S 2021 Optimizing entanglement generation and distribution using genetic algorithms *Quantum Sci. Technol.* **6** 035007
[24] Avis G, da Silva F F, Coopmans T, Dahlberg A, Jirovská H, Maier D, Rabbie J, Torres-Knoop A and Wehner S 2023 Requirements for a processing-node quantum repeater on a real-world fiber grid *npj Quantum Inf.* **9** 100

[25] Chia N-H, Chien C-H, Chung W-H and Kuo S-Y 2012 Quantum blind computation with teleportation-based computation *2012 Ninth Int. Conf. on Information Technology-New Generations* (IEEE) pp 769–74
[26] Gottesman D and Chuang I L 1999 Demonstrating the viability of universal quantum computation using teleportation and single-qubit operations *Nature* **402** 390–3
[27] Mylavarapu G, Ghosh S, Hens C, Chakrabarty I and Mitra S 2025 Teleportation fidelity of quantum repeater networks *Phys. Rev. A* **112** 032618
[28] Horodecki M, Horodecki P and Horodecki R 1999 General teleportation channel, singlet fraction and quasidistillation *Phys. Rev. A* **60** 1888
[29] Hensen B *et al* 2015 Loophole-free bell inequality violation using electron spins separated by 1.3 kilometres *Nature* **526** 682–6
[30] Kamin L, Shchukin E, Schmidt F and van Loock P 2023 Exact rate analysis for quantum repeaters with imperfect memories and entanglement swapping as soon as possible *Phys. Rev. Res.* **5** 023086
[31] Bennett C H, Brassard G, Crépeau C, Jozsa R, Peres A and Wootters W K 1993 Teleporting an unknown quantum state via dual classical and Einstein-Podolsky-Rosen channels *Phys. Rev. Lett.* **70** 1895
[32] Pfaff W *et al* 2014 Unconditional quantum teleportation between distant solid-state quantum bits *Science* **345** 532–5
[33] Chandra A, Dai W and Towsley D 2022 Scheduling quantum teleportation with noisy memories *2022 IEEE Int. Conf. on Quantum Computing and Engineering (QCE)* pp 437–46
[34] da Silva F F, Avis G, Slater J A and Wehner S 2024 Requirements for upgrading trusted nodes to a repeater chain over 900 km of optical fiber *Quantum Sci. Technol.* **9** 045041
[35] Coopmans T *et al* 2021 Netsquid, a network simulator for quantum information using discrete events *Commun. Phys.* **4** 164
[36] Shor P W and Preskill J 2000 Simple proof of security of the bb84 quantum key distribution protocol *Phys. Rev. Lett.* **85** 441
[37] Bernardes N K, Praxmeyer L and van Loock P 2011 Rate analysis for a hybrid quantum repeater *Phys. Rev. A* **83** 012323
[38] Brand S, Coopmans T and Elkouss D 2020 Efficient computation of the waiting time and fidelity in quantum repeater chains *IEEE J. Sel. Areas Commun.* **38** 619–39
[39] Li B, Coopmans T and Elkouss D 2021 Efficient optimization of cutoffs in quantum repeater chains *IEEE Trans. Quantum Eng.* **2** 1–15
[40] Collins O, Jenkins S, Kuzmich A and Kennedy T 2007 Multiplexed memory-insensitive quantum repeaters *Phys. Rev. Lett.* **98** 060502
[41] Duan L-M, Lukin M D, Cirac J I and Zoller P 2001 Long-distance quantum communication with atomic ensembles and linear optics *Nature* **414** 413–8
[42] Simon C, De Riedmatten H, Afzelius M, Sangouard N, Zbinden H and Gisin N 2007 Quantum repeaters with photon pair sources and multimode memories *Phys. Rev. Lett.* **98** 190503
[43] Jiang L, Taylor J and Lukin M 2007 Fast and robust approach to long-distance quantum communication with atomic ensembles *Phys. Rev. A* **76** 012301
[44] Sangouard N, Simon C, de Riedmatten H and Gisin N 2011 Quantum repeaters based on atomic ensembles and linear optics *Rev. Mod. Phys.* **83** 33–80
[45] Wu Y, Liu J and Simon C 2020 Near-term performance of quantum repeaters with imperfect ensemble-based quantum memories *Phys. Rev. A* **101** 042301
[46] Sangouard N, Dubessy R and Simon C 2009 Quantum repeaters based on single trapped ions *Phys. Rev. A* **79** 042340
[47] Zwerger M, Lanyon B P, Northup T E, Muschik C A, Dür W and Sangouard N 2017 Quantum repeaters based on trapped ions with decoherence-free subspace encoding *Quantum Sci. Technol.* **2** 044001
[48] Lloyd S, Shahriar M, Shapiro J and Hemmer P 2001 Long distance, unconditional teleportation of atomic states via complete bell state measurements *Phys. Rev. Lett.* **87** 167903
[49] Asadi F K, Lauk N, Wein S, Sinclair N, O'Brien C and Simon C 2018 Quantum repeaters with individual rare-earth ions at telecommunication wavelengths *Quantum* **2** 93
[50] Childress L, Taylor J, Sørensen A S and Lukin M 2006 Fault-tolerant quantum communication based on solid-state photon emitters *Phys. Rev. Lett.* **96** 070504
[51] Liorni C, Kampermann H and Bruß D 2021 Quantum repeaters in space *New J. Phys.* **23** 053021
[52] Azuma K, Tamaki K and Lo H-K 2015 All-photonic quantum repeaters *Nat. Commun.* **6** 6787
[53] Krutyanskiy V *et al* 2023 Entanglement of trapped-ion qubits separated by 230 meters *Phys. Rev. Lett.* **130** 050803
[54] Krutyanskiy V, Meraner M, Schupp J, Krcmarsky V, Hainzer H and Lanyon B P 2019 Light-matter entanglement over 50 km of optical fibre *npj Quantum Inf.* **5** 72
[55] Krutyanskiy V, Canteri M, Meraner M, Krcmarsky V and Lanyon B 2024 Multimode ion-photon entanglement over 101 kilometers *PRX Quantum* **5** 020308
[56] van Dam J, Avis G, Propp T B, da Silva F F, Slater J A, Northup T E and Wehner S 2024 Hardware requirements for trapped-ion-based verifiable blind quantum computing with a measurement-only client *Quantum Sci. Technol.* **9** 045031
[57] Beauchamp T R, Jirovská H, Gauthier S and Wehner S 2025 A modular quantum network architecture for integrating network scheduling with local program execution (arXiv:2503.12582)
[58] Stephenson L, Nadlinger D, Nichol B, An S, Drmota P, Ballance T G, Thirumalai K, Goodwin J F, Lucas D M and Ballance C 2020 High-rate, high-fidelity entanglement of qubits across an elementary quantum network *Phys. Rev. Lett.* **124** 110501
[59] Gauthier S, Vardoyan G and Wehner S 2023 An architecture for control of entanglement generation switches in quantum networks *IEEE Trans. Quantum Eng.* **4** 1–17
[60] Herbauts I, Blauensteiner B, Poppe A, Jennewein T and Huebel H 2013 Demonstration of active routing of entanglement in a multi-user network *Opt. Express* **21** 29013–24
[61] Ursin R *et al* 2007 Entanglement-based quantum communication over 144 km *Nat. Phys.* **3** 481–6
[62] Yin J *et al* 2017 Satellite-based entanglement distribution over 1200 kilometers *Science* **356** 1140–4
[63] Werner R F 1989 Quantum states with Einstein-Podolsky-Rosen correlations admitting a hidden-variable model *Phys. Rev. A* **40** 4277
[64] Munro W J, Azuma K, Tamaki K and Nemoto K 2015 Inside quantum repeaters *IEEE J. Sel. Top. Quantum Electron.* **21** 78–90
[65] Bennett C H, DiVincenzo D P, Smolin J A and Wootters W K 1996 Mixed-state entanglement and quantum error correction *Phys. Rev. A* **54** 3824
[66] Azuma K, Economou S E, Elkouss D, Hilaire P, Jiang L, Lo H-K and Tzitrin I 2023 Quantum repeaters: from quantum networks to the quantum internet *Rev. Mod. Phys.* **95** 045006

[67] Barrett S D and Kok P 2005 Efficient high-fidelity quantum computation using matter qubits and linear optics *Phys. Rev. A* **71** 060310
[68] Bruzewicz C D, Chiaverini J, McConnell R and Sage J M 2019 Trapped-ion quantum computing: progress and challenges *Appl. Phys. Rev.* **6** 021314
[69] Humphreys P C, Kalb N, Morits J P, Schouten R N, Vermeulen R F, Twitchen D J, Markham M and Hanson R 2018 Deterministic delivery of remote entanglement on a quantum network *Nature* **558** 268–73
[70] Kalb N, Reiserer A A, Humphreys P C, Bakermans J J, Kamerling S J, Nickerson N H, Benjamin S C, Twitchen D J, Markham M and Hanson R 2017 Entanglement distillation between solid-state quantum network nodes *Science* **356** 928–32
[71] Pascoletti A and Serafini P 1984 Scalarizing vector optimization problems *J. Optim. Theory Appl.* **42** 499–524
[72] Schaffer J D 1985 Some experiments in machine learning using vector evaluated genetic algorithms *Vanderbilt University Tech. Rep.*
[73] Prielinger L, Inesta A G and Vardoyan G 2025 Surrogate-guided optimization in quantum networks *npj Quantum Inf.* **11** 89
[74] Drmota P *et al* 2023 Robust quantum memory in a trapped-ion quantum network node *Phys. Rev. Lett.* **130** 090803
[75] Ghadimi M, Connell S, Scarabel J, Shimizu K, Streed E and Lobino M 2019 Towards long-distance quantum communication using trapped ions and frequency qubits *AOS Australian Conf. on Optical Fibre Technology (ACOFT) and Australian Conf. on Optics, Lasers and Spectroscopy (ACOLS) 2019* vol 11200 (SPIE) pp 69–70
[76] Inlek I V, Crocker C, Lichtman M, Sosnova K and Monroe C 2017 Multispecies trapped-ion node for quantum networking *Phys. Rev. Lett.* **118** 250502
[77] Higgins G, Li W, Pokorny F, Zhang C, Kress F, Maier C, Haag J, Bodart Q, Lesanovsky I and Hennrich M 2017 Single strontium Rydberg ion confined in a Paul trap *Phys. Rev. X* **7** 021038
[78] Northup T E, Lanyon B P and Krutyanskiy V 2025 private communications
[79] Häffner H *et al* 2005 Robust entanglement *Appl. Phys. B* **81** 151–3
[80] Rosenband T *et al* 2007 Observation of the s 0 1→ p0 3 clock transition in al+ 27 *Phys. Rev. Lett.* **98** 220801
[81] Home J P, McDonnell M, Szwer D, Keitch B, Lucas D, Stacey D and Steane A 2009 Memory coherence of a sympathetically cooled trapped-ion qubit *Phys. Rev. A* **79** 050305
[82] Maiti S, Avis G, Kar S and Wehner S 2026 *Supplementary Notes: Requirements for Teleportation in an Intercity Quantum Network* (https://doi.org/10.5281/zenodo.22216782)
[83] Maiti S 2026 Code underlying the paper: Requirements for teleportation in an intercity quantum network (available at: https://gitlab.tudelft.nl/wehner-research/teleportation_requirements_paper.git)
[84] Schupp J, Krcmarsky V, Krutyanskiy V, Meraner M, Northup T and Lanyon B 2021 Interface between trapped-ion qubits and traveling photons with close-to-optimal efficiency *PRX Quantum* **2** 020331
[85] Maiti S 2026 Data underlying the paper: Requirements for teleportation in an intercity quantum network *Dataset, 4TU.ResearchData* (https://doi.org/10.4121/6b7d42d3-ff78-4d64-bc9a-449480cc8550)